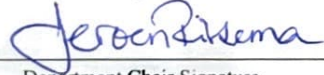**Theresa Juanita-Marie Casselman**

The effects of microbial iron reduction and silica on green rust in banded iron formations

submitted in partial fulfillment of the requirements for the degree of
Master of Science in Earth and Environmental Sciences
Department of Earth and Environmental Sciences
The University of Michigan

Accepted by:

Signature	Jena E Johnson	5/09/2024
	Name	Date
Signature	Rose M. Cory	5/15/2024
	Name	Date
Department **Chair** Signature	JEROEN RITSEMA	5/20/24
	Name	Date

I hereby grant the University of Michigan, its heirs and assigns, the non-exclusive right to reproduce and distribute single copies of my thesis, in whole or in part, in any format. I represent and warrant to the University of Michigan that the thesis is an original work, does not infringe or violate any rights of others, and that I make these grants as the sole owner of the rights to my thesis. I understand that I will not receive royalties for any reproduction of this thesis.

☑ Permission granted.

☐ Permission granted to copy after: _____

☐ Permission declined.

_____
Author Signature

Earth and Environmental Sciences
MUNIVERSITY OF MICHIGAN

The effects of microbial iron reduction and silica on green rust in banded iron formations

Abstract

The geochemical composition of Earth's oceans was different from that of modern oceans prior to the Great Oxidation Event (2.4 Ga), with negligible free oxygen and abundant iron dissolved in both water columns and sediments. Deposition of these anoxic, iron-rich marine sediments, mainly in the Archean eon (2.5-4 Ga), gave rise to banded iron formations (BIFs). The first life on Earth, in the form of microbes, is thought to have evolved under the same conditions as BIFs. Thus, BIFs may contain a record of those microbes' metabolisms. Archean BIFs are composed of iron-rich oxides, carbonates, and silicates. These minerals are thought to be secondary minerals altered from an unknown primary phase by a combination of abiotic and possibly biotic processes. One proposed primary BIF phase is carbonate green rust, an Fe(II,III) salt that could have been transformed via microbial iron reduction into Fe(II)-rich secondary BIF minerals. The two main goals of this study were 1) to explore the effects of microbial iron reduction on green rust and 2) to explore the effects of silica on green rust transformation. Silica concentrations are thought to have been high in Archean oceans, but silica is also known to stabilize green rust and slow its transformation into other mineral phases, raising questions about how the high marine silica and hypothesized green rust BIF sediments interacted to form the BIF minerals seen today. Using scanning electron microscopy, Raman spectroscopy, and X-ray diffraction, we found that after hydrothermal aging, green rust transformed into siderite and subsequently magnetite, a common BIF carbonate and oxide, respectively, independent of the presence of *S. putrefaciens*. These results provide support for green rust as a primary BIF phase. However, the results suggest that siderite is not a reliable biosignature in the context of green rust as it forms in both biotic and abiotic conditions. Siderite was only seen in the absence of silica, while iron-silica coprecipitates dominated when silica was present. Our findings potentially constrain BIF mineral formation conditions, suggesting that iron silicates were the predominant minerals forming when marine silica concentrations were high and iron carbonates appeared only when silica levels were low. Further exploration of biotic and abiotic iron reduction pathways under these conditions would improve our understanding of early life on Earth and could help identify signs of past or present life elsewhere in our solar system and beyond.

Table of Contents

1   Intro

Life on Earth is thought to have first evolved as early as 3.5 Ga in the form of microorganisms (Schopf et al. 1993, 2018). Fossil evidence of early life is scarce because these microscopic microorganisms, or microbes, are rarely preserved as microfossils and the rocks in which they were deposited have undergone extensive diagenetic and metamorphic changes in the intervening millennia. The Archean eon (2.5-4 Ga), during which Earth's first lifeforms emerged, was filled with metamorphic activity (Kröner, 1985), making any sort of preservation difficult but not impossible. To determine whether some record of early life has been preserved in Archean rocks in spite of these challenges, an understanding of the marine environment in which these rocks formed is needed.

The conditions of Earth's oceans at this time were very different from the modern Earth, predating the Great Oxidation Event (GOE) of 2.4 Ga when our atmosphere became oxygenated (Lyons et al. 2014). Pre-GOE oceans were anoxic and ferruginous, rich in ferrous iron that was largely emitted by hydrothermal vents (Kump and Seyfried, 2005). The pH of Archean oceans is thought to have been circumneutral or slightly acidic, at 6.5-7.0 (Halevy and Bachan, 2017). Dissolved inorganic carbon (DIC) was present at a higher concentration than in modern oceans at around 10 mM (Halevy and Bachan, 2017). Silica is also believed to have been more abundant in the Archean, with estimated levels ranging from 0.5-2.0 mM (Siever, 1992; Maliva et al. 2005; Stefurak et al 2015). It was under these conditions that banded iron formations (BIFs) formed.

The majority of BIFs formed in the anoxic conditions of the Earth pre-GOE, between 3.8 and 2.45 Ga (Bekker et al. 2010). These sedimentary rock formations are comprised mainly of Fe(II)-rich carbonates, Fe(II,III) oxides, and silicates that often contain a combination of ferrous and ferric iron. Common BIF minerals include the ferrous iron carbonate siderite ($FeCO_3$), the mixed-valence iron oxide magnetite (Fe_3O_4), and mixed-valence iron silicate cherts such as greenalite (($Fe(II,III)_{2-3}Si_2O_5(OH)_4$). These minerals are generally thought to be secondary in nature, having been formed through diagenetic or metamorphic processes following initial deposition of Archean sediments (Kaufman et al. 1990; Rasmussen et al. 2014; Rasmussen and Muhling, 2018; Tosca et al. 2019; Rasmussen et al. 2021). The primary phase(s) of BIFs has been proposed by some researchers to be a ferric oxyhydroxide such as ferrihydrite (James, 1954; Beukes and Gutzmer, 2008; Bekker et al. 2010, 2014; Konhauser et al. 2017) or hematite (Sun et al. 2015), while others have shown that many Fe(III) oxides are secondary in BIFs and posit that a partially or fully reduced iron mineral phase would have been more likely given the reducing conditions of Archean oceans (Kaufman et al. 1990; Rasmussen et al. 2014; Rasmussen et al. 2016; Halevy et al. 2017; Tosca et al. 2019). Identifying the primary BIF phase(s) would help elucidate whether early microbes were involved in BIF genesis, and if some record of these microbes or their metabolisms has been preserved in BIFs despite the subsequent alterations.

Since BIFs are rich in both ferrous and ferric iron, investigations into potential microbial metabolisms involved in BIF genesis have focused on Fe(II) oxidation (Walker, 1984; Widdel et al. 1993; Kappler et al. 2005; Konhauser et al. 2007; Posth et al. 2010; Zhou et al. 2024) and Fe(III) reduction (Heimann et al. 2010; Craddock and Dauphas, 2011; Posth et al. 2103; Konhauser et al. 2017). Microbe-driven Fe(II) oxidation likely occurred higher up in the water column, possibly accompanied by abiotic photooxidation (Braterman et al. 1983). In the reducing environment near the base of the water column and in the sediment pore waters, Fe(III) reduction was the likely metabolism carried out by microbes in

Archean sediments. Dissimilatory iron reduction (DIR) reduces ferric iron while oxidizing a different compound, often a carbon source such as lactate or acetate (Lovley and Phillips, 1988). DIR of Fe(III) or Fe(II,III) phases could have produced fully reduced iron carbonates such as siderite (Klein and Beukes, 1989; Johnson et al. 2008) or partially reduced iron oxides or silicates such as magnetite (Johnson et al. 2008; Craddock and Dauphas, 2011) or greenalite (Fischer and Knoll, 2009; Rasmussen et al. 2017; Johnson et al. 2018), all minerals commonly found in BIFs.

A 2022 study by Nims and Johnson explored DIR of ferrihydrite as a process to promote the hypothesized conversion of a ferric primary phase to the more reduced secondary minerals seen in BIFs. Prior studies have also looked at DIR of ferric oxides but did not replicate the silica-rich Archean ocean conditions or characterize the secondary product mineralogy (Bae and Lee, 2013; Etique et al. 2016; Han et al. 2020; O'Loughlin et al. 2019; Salas et al. 2009; Zegeye et al. 2010). Silica has been shown to impede both DIR (Wu et al. 2009) and abiotic Fe(III) mineral reduction (Cornell et al. 1987; Jones et al. 2009) and has therefore been omitted from many BIF studies, but these silica-free conditions are then poor replicas for Archean environments because it is generally agreed that Archean oceans were silicious (Siever, 1992; Maliva et al. 2005; Stefurak et al 2015).

Iron silicates are an important early-preserved constituent of BIF cherts, but it is unknown whether they are primary precipitates that formed in the water column or if they are a product of DIR or other post-depositional reactions. Percak-Dennett et al. (2011) looked at microbial DIR of an Fe(III)-silica coprecipitate but focused on the iron isotopic signatures; they simply noted that the reduced iron-silica precipitate products were all amorphous. Results of ferrihydrite DIR by Nims and Johnson (2022) showed putative iron silicates and calcium carbonates rather than iron carbonates, with a final assemblage of remaining ferric oxides. The authors hypothesized that calcium carbonates formed instead of iron carbonates due to a low solution ratio of Fe:Ca because the initial composition of the system was 1.5 mM ferrihydrite and 10 mM Ca. The abundance of Fe(III) oxides that remained after ferrihydrite DIR did not resemble BIF mineral assemblages and suggests that an Fe(II,III) mineral phase may have been a more likely precursor.

Ferrihydrite would have descended through an increasingly reducing water column and is unlikely to have reached the ocean floor without undergoing some reduction (Zegeye et al. 2012; Chorney and Chemtob, 2023). Aqueous Fe(II) in the water column could have reacted with the ferrihydrite to produce green rust, an Fe(II,III) hydroxy-anion salt (Sumoondur et al. 2008). There are three possible anion constituents of green rust: chloride ($[Fe^{2+}_3Fe^{3+}(OH^-)_8] \cdot [Cl \cdot 2H_2O]$), sulfate ($[Fe^{2+}_4Fe^{3+}_2(OH^-)_{12}] \cdot [SO_4 \cdot 2H_2O]$), and carbonate ($[Fe^{2+}_4Fe^{3+}_2(OH^-)_{12}] \cdot [CO_3^{2-} \cdot 2H_2O]$) (Abdelmoula et al. 1998). Chloride green rust is the least stable of the three and sulfate green rust is unlikely to have been abundant in Archean oceans, given that sulfate concentrations were lower than chloride or carbonate (Halevy et al. 2017; Chorney and Chemtob, 2023). Carbonate green rust was the most likely precursor BIF phase because it is more stable than its chloride counterpart (Chorney and Chemtob, 2023) and carbonate concentrations were high in Archean waters (Halevy and Bachan, 2017). Notably, carbonate green rust was observed to form secondarily from initial ferrihydrite as the oxyhydroxide gets reduced by Fe(II) in a ferruginous modern lake analogue for Archean oceans (Zegeye et al 2012). Green rust has also been proposed as a primary BIF phase, forming when iron is partially oxidized under Fe(II)-rich conditions (Halevy et al. 2017). The persistence of ferric oxides following ferrihydrite DIR (Nims and Johnson, 2022) provides another compelling reason to consider how the products of DIR change when given a mixed-valence iron phase like green rust instead of ferrihydrite.

This study aims to build upon the results of Nims and Johnson by exploring the products of the microbial DIR of carbonate green rust using the model iron-reducing microbe *Shewanella putrefaciens*. Reactions were carried out in solutions replicating Archean seawater conditions, using lactate as the electron donor and carbon source and carbonate green rust as the electron acceptor. Following the results of Nims and Johnson (2022), we excluded Ca^{2+} from the experimental solution to study iron products in the absence of calcium carbonates. We compared the products of green rust DIR with abiotic green rust transformation, to determine if any minerals or mineral combinations could represent a biosignature of Archean lifeforms. We also explored the effects of silica on this system by including 1 mM dissolved silica in one set of replicates and excluding it from an otherwise identical set. Our findings contribute to the growing body of research exploring the likelihood of green rust as a primary BIF phase. Through this study, we aim to improve the field's understanding of the roles played by iron-reducing microbes and silica in the genesis of Archean BIF minerals and whether these minerals contain a record of early life on Earth.

2   Methods

2.1 Experimental setup

2.1.1   *Experimental overview*

This experiment was designed to compare the influences of two main factors on the degradation of green rust into potential BIF secondary minerals: the presence of iron-reducing microbes and the presence of 1mM silica. To this end, we prepared three treatments with 1 mM silica added to the experimental media (GR+Si) and three without (GR-Si). Within each set of experiments, iron-reducing microbes were added to two treatments and the third was used as an abiotic, microbe-free control. All six experiments were set up in 60 mL borosilicate glass serum bottles and contained 60mL reaction volume comprised of 10mM green rust carbonate (see section 2.1.2 below), artificial Archean seawater (see section 2.1.3), and with the exception of the abiotic controls, *Shewanella putrefaciens* CN32 (section 2.1.4). Once all components were prepared and added, the six serum bottles were incubated for 15 days at room temperature (21-22 °C), wrapped in aluminum foil to block out light and prevent the possible effects of photooxidation, and agitated on a shaker at 150 rpm. Subsequently, we subsampled the low-temperature solid products and then aged the experiments at 80 °C for 10 days to promote crystallization.

All work carried out on the benchtop followed aseptic technique using a Bunsen burner. All glassware used in this experiment was triple-washed, soaked overnight in 10% hydrochloric acid, triple-washed again, and then autoclaved at 121°C prior to use to minimize risk of contamination. Surfaces inside the glovebox were cleaned with 70% ethanol where possible.

2.1.2   *Primary substrate – Green rust carbonate*

The electron acceptor used in this experiment to represent the initial solid phase in Archean marine sediments was carbonate green rust. We prepared this mixed-valence iron phase by combining 66 mM anhydrous ferric chloride with 300 mM ferrous chloride tetrahydrate to reach a ~3:1 ratio of $Fe^{2+}:Fe^{3+}$

(Ruby et al. 2006). To reverse any prior oxidation and ensure reducing conditions in the ferrous chloride during preparation, 60 mg elemental iron (Fe^0) was added to the acidic ferrous chloride stock, producing H_2. Next, we added 100 mM sodium carbonate to the combined iron chlorides to provide the carbonate component of green rust, again in a 3:1 ratio of $Fe^{2+}:CO_3^{2-}$. The reaction of the mixed iron chlorides with the sodium carbonate occured spontaneously and rapidly, beginning within seconds of combination. All powders were weighed on the benchtop, then transferred into the anoxic glovebox and dissolved in degassed Milli-Q water. Once we combined the ferrous and ferric chlorides and sodium carbonate and green rust began to precipitate, the solution was left to sit for 30 minutes to allow the reaction to continue but preclude degradation; even in the anoxic glovebox, green rust is volatile enough that it will degrade within hours. Following the 30-minute incubation, we washed the green rust precipitate three times in degassed Milli-Q water to remove any excess salts, then kept it in the glovebox for 1-2 hours until the experiment was ready to proceed. We analyzed a small sample of the precipitate via SEM microscopy and Raman spectroscopy to confirm that the precipitate was indeed green rust (Fig. 2).

2.1.3   Media – Artificial Archean seawater

The biogeochemical matrix of Archean oceans remains unknown, but the likely components and their concentrations have been constrained to relatively narrow ranges. The media used in this experiment replicated the artificial seawater originated by Kester et al. (1967) for modern artificial seawater, adapted by Percak-Dennett et al. (2011) for artificial Archean seawater (AAS). It includes some modifications made by Nims and Johnson (2022), which sought to incorporate more recent estimates for Archean seawater and include chemical constituents required for microbe survival. The resulting AAS used here is detailed in Table 1. We modified the recipe followed by Nims and Johnson (2022) to include a low concentration of phosphate in the media to promote bacterial growth. However, vivianite formation is a concern due to the tendency of phosphate to precipitate with reduced iron (Cosmidis et al 2014; Nims and Johnson, 2022). We initially added 50 µM of KH_2PO_4 but observed some vivianite production. Reducing the concentration to 10 µM proved to be sufficient for *S. putrefaciens* activity while avoiding vivianite formation. Nims and Johnson added calcium into their AAS and observed extensive calcium carbonate formation and a lack of iron carbonates in their precipitates. We wanted to determine whether iron carbonates can form in AAS conditions, so we excluded calcium from the AAS used in this study to avoid repeating this result. AAS reagents were prepared and stored in anoxic conditions where possible, with exceptions including the trace minerals (Widdel et al. 1983), vitamins (Balch and Wolfe, 1976), and amino acids (Myers and Nealson, 1990), which required refrigeration and were added to the AAS in such small quantities (1 mL into 1 L) that they did not introduce a significant amount of oxygen. The sodium, magnesium, potassium, and ammonium chlorides were brought into the anoxic glovebox in powder form, then dissolved into anoxic Milli-Q water, which had been autoclaved prior to being degassed to reduce the possibility of contamination. The other AAS components were added in the order listed in Table 1 using a serological pipette or 1000 µL pipettor depending on the volume required, while the 1L bottle spun on a stir plate at ambient temperature (25°C). Once all AAS constituents had been added, the solution was adjusted from its starting pH of around 8.5 to circumneutral pH using 1M HCl. We transferred a 200 mL aliquot of AAS to a new bottle, added 1 mM sodium metasilicate, and spun the solution overnight to ensure silica depolymerization. This aliquot was then used for the green rust plus silica (GR+Si) condition, while the original AAS was used for the green rust minus silica condition (GR-Si). Seawater salts and green rust were added in the anoxic environment of an MBraun LABstar glovebox with oxygen levels < 0.1 ppm.

Table 1   Artificial Archean seawater components and concentrations

Salts		Molar mass	Final [ ] (mM)	Amount to add
	NaCl	58.44	400	23.38 g
	MgCl$_2$ · 6H$_2$O	203.3	20	4.066 g
	KCl	74.55	9	0.6710 g
	NH$_4$Cl	53.49	1	0.0535 g
Stock solutions		**Stock [ ]**		
	NaHCO$_3$ (from 1 M stock)	1 M	5	5 mL
	KH$_2$PO$_4$ (from 10 mM stock)	10 mM	0.005 (5 uM)	0.5 mL
	Sodium lactate	2 M	30	15 mL
	Trace minerals, filtered	-	See Table S1	1 mL
	Vitamin mix, filtered	-	See Table S2	1 mL
	Amino acid mix, filtered	-	See Table S3	1 mL
	Autoclaved, anoxic Milli-Q water	-	-	976.5 mL
Total				**1 L**
	If adding sodium metasilicate	122.06	1	1 mL

2.1.4   *Microbes – Shewanella putrefaciens*

A model iron-reducing bacterial species, *Shewanella putrefaciens* CN32, was grown from a freezer stock in tryptic soy broth (TSB). The TSB was prepared by dissolving 15 g of TSB powder in 500 mL of Milli-Q water and heating the mixture to 121°C for one hour to prevent contamination. The TSB was then divided into five 250 mL Erlenmeyer flasks in volumes of 100 mL each, poured under sterile conditions. Once the TSB cooled to 30°C, *S. putrefaciens* CN32 was inoculated in four of the flasks, while one flask was reserved as an abiotic control. All five flasks were incubated at room temperature (21-22°C) on a shaker moving at 150 rpm for 23 hours until the optical density was 0.667 when measured at 600 nm on a spectrophotometer. The microbes were then spun down in a centrifuge at 2000 rpm for 5 minutes, combined into one centrifuge 50mL tube, spun down again to remove excess TSB, and resuspended in 5 mL TSB. We added 1 mL of this microbe-rich media via syringe to four of the sealed 60 mL serum bottles containing green rust and AAS, as described in section 2.1.1. The bottles were sealed with rubber stoppers and metal crimpers, removed from the glovebox, and the microbes were added through the stoppers via syringe.

2.1.4   *Hydrothermal aging to simulate diagenesis and promote crystallization*

Following the 15 days of incubation at room temperature, we transferred the serum bottles into the glovebox, unsealed them, and extracted a precipitate subsample from each experiment for further analysis. The bottles were then stoppered and crimped again and placed in an oven at 80°C for 10 days of hydrothermal aging, in the dark with no agitation. These conditions replicate early diagenesis and should accelerate crystallization of any minerals that formed during the initial 15 days. At the end of the ten days at 80°C, precipitate samples were again extracted for further analysis in the anoxic glovebox conditions.

2.2 Assays

2.2.1   pH

Archean oceans are thought to have had a pH of around 6.5-7 (Halevy and Bachan, 2017). A pH of 7 is more favorable than 6.5 for *S. putrefaciens* and green rust is more stable at higher pH and dissolved into the AAS immediately at a pH of 6.5, so experimental conditions were set at a circumneutral pH of around 7. We took pH measurements throughout the experiment using a ThermoFisher Orion Star A221 portable pH meter that was calibrated regularly using the ThermoFisher protocol and standards. Before beginning the experiment, the AAS was adjusted to circumneutral pH down from ~8.5 using anoxic 1 M HCl. Once green rust was added, the system was left to equilibrate for 45 minutes, then adjusted down again to pH 7 in each of the 60 mL reaction vessels. pH was then measured, but not adjusted, on days 3, 5, 7, 10, and 15.

2.2.2   Ferrozine assay

The ferrozine assay is a colorimetric assay used to measure the concentrations of Fe^{2+} and total iron in solution (Stookey, 1970; Voillier et al. 2000). After the AAS and green rust were combined, given time to equilibrate, and adjusted to circumneutral pH, 1 mL of solution from each serum bottle was passed through a 0.2 µM filter to remove any small particles of solid-phase iron and diluted 100X in 0.5M HCl to bring the Fe^{2+} and total iron absorbances to within a readable range when run through the ferrozine assay on a spectrophotometer. Initial Fe^{2+} absorbances were taken after adding ferrozine reagent to each diluted sample, which binds to ferrous iron and turns purple. Hydroxylamine HCl was added, left to sit for 10 minutes, followed by the addition of 200 µL of ammonium acetate; these two reagents bind to any ferric iron in solution, turning it purple as well, allowing total iron absorbance to be measured on the ThermoScientific Genesys 50 UV-Visible spectrophotometer at the 562 nm wavelength. Following this initial day 1 assay, iron speciation data were collected via ferrozine assays on days 3, 5, 7, 10, and 15 at the same time pH was measured. To avoid having to unseal the serum bottles and risk possible oxygen contamination, 1.5 mL of solution was extracted through the rubber stopper using a syringe while in the glovebox. Filtration, dilution, and the assay steps were kept the same as above.

2.2.3   Silica-molybdate assay

The silica-molybdate assay is a colorimetric assay that binds to silica ions and uses ammonium molybdate as the colorimetric reagent (Strickland and Parsons, 1972). This assay, in which first HCl and oxalic acid are added, then ammonium molybdate and amino-naphthol-sulfonic acid, involves ammonium molybdate binding to silica ions and turning blue, enabling silica concentration to be measured via absorbance on the spectrophotometer at the 640 nm wavelength. As with pH and iron levels, silica levels were measured in the green rust replicates with 1 mM silica (GR+Si) using this assay on days 1, 3, 5, 7, 10, and 15, and on days 1 and 15 for the green rust replicates that excluded silica (GR-Si) to confirm the absence of silica. Sample solutions were again passed through a 0.2 µM filter to ensure that only silica that was fully in solution was measured.

2.3 Microscopy

2.3.1   *Scanning electron microscopy*

A JEOL JSM-7800FVL scanning electron microscope (SEM) housed in the Electron Microbeam Analysis Lab (EMAL) at the University of Michigan was used to analyze the morphology and elemental composition of each of the experimental precipitates. We triple-washed 1 mL of precipitate from each of the six serum bottles and then diluted them 10X. A few drops (~20 uL) of sample were pipetted onto carbon tape-wrapped metal stubs and left to dry in the glovebox for one hour. We then coated the samples in gold using the Denton Desk II gold sputter coater to provide conductivity for the SEM electron beam to be able to work. This gold coating, applied for 90 seconds at 50 millitorr and 40 milliamps to achieve a coating 300 Å thick, also helped seal the samples against oxidation. For general imaging, the electron beam was set to 10 kV with a probe current of 8 amps. The beam was adjusted to 15 kV to increase sensitivity when obtaining point spectra for elemental composition analysis of different morphology types using an Oxford XMaxN 80mm² silicon-drift energy-dispersive X-ray spectrometer (SEM-EDS), also located in EMAL. We used Oxford Aztec software (version 3.3) to visualize the EDS point spectra and map data. SEM imaging and SEM-EDS were carried out for all six precipitates at the end of the initial 15-day incubation and again following the 10 days of hydrothermal aging.

2.3.2   *Raman microprobe spectroscopy*

Raman spectroscopy data were obtained using an XploRA PLUS Raman spectrometer in combination with an Olympus BX41 microscope housed in the Microbe-Mineral Lab at the University of Michigan. This system enables acquisition of a Raman spectrum on a ~1 micron spot. Samples were prepared under anoxic conditions using triple-washed but undiluted precipitates to optimize Raman analysis. We spun down 1 mL of washed, undiluted precipitate, removed the supernatant, and pipetted 40 μL of precipitate onto a glass slide. A coverslip was sealed over top of the sample using clear acrylic nail polish to prevent oxidation once the sample was taken out of the glovebox. We prepared each sample immediately before use; leaving even the sealed samples in the glovebox for an extended period of time resulted in oxidation. We used a 25 mW laser at 532 nm, generally at 0.125-0.5% intensity but sometimes going as high as 10%. We found that 50X magnification, 20-30 seconds of laser acquisition, and 5 accumulations worked best for most samples, both before and after aging.

3 Results

3.1 Solution chemistry

3.1.1 pH

Solution pH values followed a similar trend for all six samples independent of the presence of microbes or silica. Sample solutions started at a circumneutral pH after adjustment (Table 2, Day 1), increased towards a pH of 7.8-7.9 through day 5, and plateaued through day 10. The pH dropped to around 7.5 between days 10 and 15 for all samples except two of the GR+Si treatments; one of the microbial treatments (GR+Si M) and the control experiment (GR+Si C) both dropped below 7 (Table 2 and Fig. 1a). No significant differences in pH were seen between samples independent of microbe or silica content.

Table 2   Solution pH measurements

Sample	Day 1	Day 3	Day 5	Day 7	Day 10	Day 15
GR-Si 1	7.12	7.38	7.87	7.83	7.86	7.48
GR-Si 2	7.09	7.31	7.84	7.92	7.9	7.45
GR-Si C	7.14	7.43	7.91	7.89	7.9	6.79
GR+Si 1	6.99	7.6	7.73	7.71	7.81	6.94
GR+Si 2	7.08	7.52	7.85	7.76	7.56	7.48
GR+Si C	6.99	7.47	7.78	7.69	7.71	7.52

3.1.2 Silica

Solution silica levels hovered just above the detection limit from days 1-15 for the three GR-Si experiments. For the three GR+Si experiments, all three samples dropped below the starting level of 1 mM silica immediately (day 1), rose by day 3, fluctuated with no clear pattern through days 5 and 7, then rose in the case of the two GR+Si M treatments and dropped for GR+Si C, with all three remaining stable from days 10 to 15 (Table 3 and Fig. 1b). Silica levels were much higher in the GR+Si experiments than in the GR-Si condition. There was a clear difference between the GR-Si and GR+Si sample conditions, but no evident difference between microbial and abiotic conditions within the GR-Si and GR+Si experimental sets.

Table 3   Silica concentration (in mM) in solution

Sample	Day 1	Day 3	Day 5	Day 7	Day 10	Day 15
GR-Si 1	0.027					0.065
GR-Si 2	0.030					0.074
GR-Si C	0.021					0.071
GR+Si 1	0.211	0.312	0.635	0.148	0.579	0.561
GR+Si 2	0.258	0.350	0.162	0.173	0.650	0.644
GR+Si C	0.350	0.481	0.534	0.534	0.398	0.445

3.1.3   Iron

Solution concentrations of ferrous iron, Fe(II), and total iron, Fe(T) followed similar but distinguishable trends within the GR-Si and GR+Si experimental sets. Across most experiments, Fe(II) concentration fluctuated through days 1 to 7 before stabilizing from day 10 to 15, following a similar pattern between sample solutions (Table 4 and Fig. 1c). In the GR-Si condition, Fe(II) concentration was consistently higher and increased more sharply from days 5-7. Fe(II) concentration was also slightly higher in all microbial treatments compared to their respective controls. Similarly, Fe(T) was consistently higher in the GR-Si condition than GR+Si and in microbial treatments compared with their respective controls. In all six samples, Fe(T) rose from days 1-5, dipped in all but GR-Si 1 by day 7, then plateaued or rose slightly between days 7 and 15 (Table 4 and Fig. 1d). Overall, readily apparent differences were observed between the GR+Si and GR-Si conditions while there were subtle differences between microbial and control treatments for both Fe(II) and Fe(T) solution concentrations.
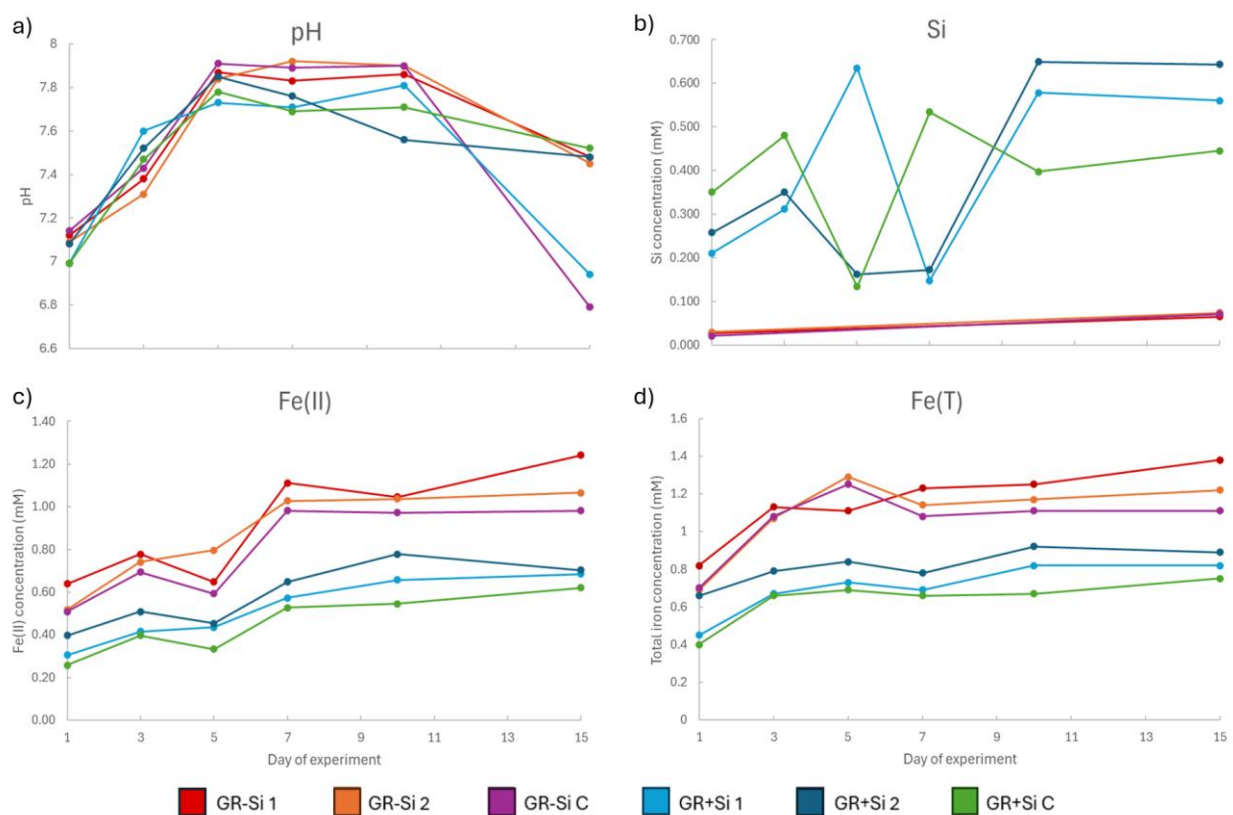

Figure 1   Solution chemistry for days 1-15 of the experiment. Panel a) shows the pH measurements, b) the silica concentration in solution, c) the Fe^{2+} concentration, and d) the total iron concentration in solution.

Table 4   Total iron and Fe(II) concentration (in mM) in solution

Sample	Day 1		Day 3		Day 5		Day 7		Day 10		Day 15	
	Fe(II)	Fe(T)	Fe(II)	Fe(T)	Fe(II)	Fe(T)	Fe(II)	Fe(T)	Fe(II)	Fe(T)	Fe(II)	Fe(T)
GR-Si 1	0.64	0.82	0.78	1.13	0.65	1.11	1.11	1.23	1.05	1.25	1.24	1.38
GR-Si 2	0.52	0.69	0.74	1.07	0.80	1.29	1.03	1.14	1.04	1.17	1.06	1.22
GR-Si C	0.51	0.7	0.69	1.08	0.59	1.25	0.98	1.08	0.97	1.11	0.98	1.11
GR+Si 1	0.30	0.45	0.42	0.67	0.43	0.73	0.57	0.69	0.66	0.82	0.68	0.82
GR+Si 2	0.40	0.66	0.51	0.79	0.45	0.84	0.65	0.78	0.78	0.92	0.70	0.89
GR+Si C	0.26	0.4	0.40	0.66	0.33	0.69	0.53	0.66	0.55	0.67	0.62	0.75

3.2 Experimental precipitates after aging at room temperature

3.2.1   *Green rust without silica*

After the samples incubated for 15 days at room temperature, we extracted precipitates and performed the first round of SEM-EDS and Raman analyses. Hexagons matching those seen in the pre-reaction green rust precipitate (Fig. 2a) were prevalent throughout SEM images for GR-Si C, often forming loose circular aggregates (Fig. 3a, b). Small spherules (Fig. 3c) and a background of curling plates resembling degrading green rust hexagons also featured frequently (Fig. 3d). The identification of the hexagons as green rust was corroborated by Raman spectra (Fig. 3e) that matched spectra of the original green rust precipitate (Fig. 2b). Raman analysis also revealed the presence of lepidocrocite an iron oxide (γ-FeO(OH)).

As shown in Figure 4, distinctive hexagonal plates at varying stages of degradation were the dominant feature (Fig. 4a, b, e) in the two GR-Si M experiments. These hexagons matched the appearance of the initial green rust precipitate (Fig. 2a), supporting an ID of green rust, further confirmed by Raman spectra (Fig. 4g) matching the initial green rust spectra (Fig. 2b). Green rust formed
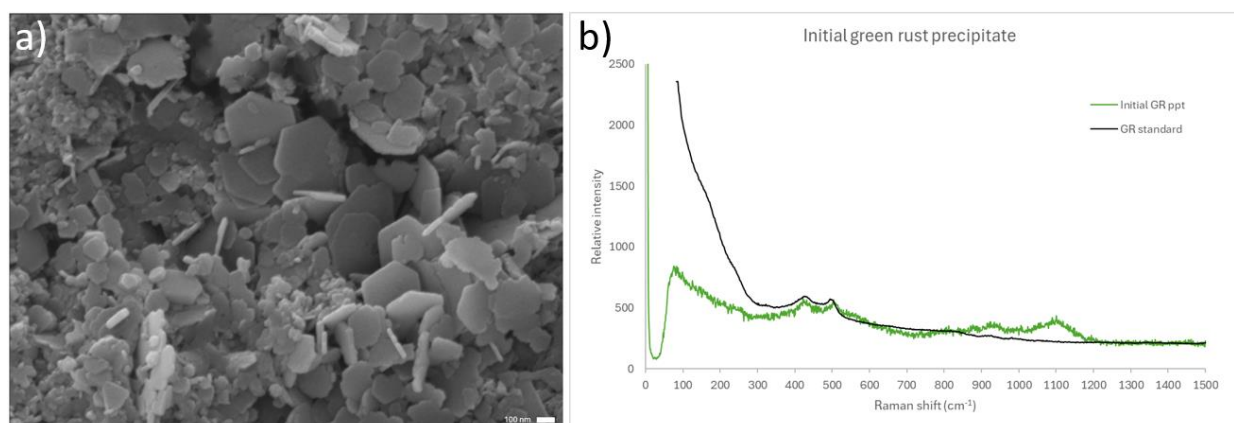

Figure 2   The initial precipitate described in section 2.1.2 was confirmed to be green rust via (a) SEM and (b) Raman spectroscopy. The morphology was confirmed to be hexagonal plates (a) characteristic of green rust and the Raman spectrum (green) generated matched a standard spectrum (black) (b).

aggregates in many instances (Fig. 4a, b) or formed a background layer of degrading hexagonal plates (Fig. 4e). SEM-EDS point spectra revealed that the hexagons (on carbon tape) predominantly showed carbon (54.5%) and oxygen (38.8%) with 2.9% total iron (Table 5). Small spherules were also present in SEM images (Fig. 4c) and several instances of an acicular morphology co-occurring with green rust were seen but could not be identified (Fig. 4d). No microbes were visible on the SEM, but we identified many spectra for cytochrome C, a hallmark of biological material, via Raman spectroscopy in the biotic precipitates (Fig. 4h).

Table 5   EDS data

Sample	Day	Morphology	C	O	Fe	Si	Fe:Si	(Fe+Mg):Si	# of sites
Initial GR	1	Hexagons	58.8	35.2	3.8				
GR-Si M	15 (pre-80°C)	Green rust aggregate	54.5	38.8	2.9	No silica content			6
	25 (post-80°C)	Hexagons	44.8	48.0	3.0				3
		Spheres	42.8	47.8	7.5				5
		Encrusted microbes	78.2	19.9	0.8				16
		Curling plates	56.4	35.8	3.0				2
GR-Si C	25 (post-80°C)	Sphere-cubes	40.0	54.9	2.6				6
		Platy aggregates	34.6	58.1	5.5				7
GR+Si M	15 (pre-80°C)	Acicular	45.2	45.0	2.9	1.4	2.1	2.3	7
		Capsules	46.6	39.9	4.7	2.7	1.7	1.9	5
		Clusters	48.3	39.6	2.4	3.8	0.6	0.9	5
	25 (post-80°C)	Amorphous	59.4	33.6	1.5	1.8	0.8	1.1	10
		Clusters	58.0	34.8	2.6	2.9	0.9	1.1	16
		Curling plates	40.5	49.1	2.5	3.2	0.8	1.0	7
		Sheet	58.7	37.4	1.3	1.5	0.8	1.1	4
		Sphere 1	55.9	37.6	5.6	0.1	48.3	49.3	6
		Sphere 2	51.4	32.9	10.2	1.4	7.1	7.3	3
GR+Si C	25 (post-80°C)	Amorphous	46.4	48.2	1.7	2.5	0.7	0.9	5
		Clusters	43.6	49.9	2.0	2.8	0.7	1.0	10
		Sheet	45.2	47.2	2.4	3.3	0.7	1.0	14

3.2.2   Green rust with silica

The main morphologies found in the GR+Si C treatment were sheets of small platy clusters (Fig. 5a, c) and curling plate aggregates (Fig. 5b, c). We found spectra matching magnetite (Fig. 5e) and goethite (α-FeO(OH)) (Fig. 5f), a polymorph of lepidocrocite (Bernal et al. 1935), via Raman spectroscopic analysis of this precipitate. A few hexagons matching the initial green rust were visible but were significantly less abundant than in either GR-Si condition.

In the GR+Si M treatments, the dominant morphologies seen via SEM were sheets of small platy clusters (Fig. 6a, c) and larger aggregates of curling hexagonal plates (Fig. 6b), as was the case for GR+Si C. Spectra for green rust were also found on the Raman microprobe (Fig. 6g). A capsule-shaped morphology was seen in several regions throughout the sample (Fig. 6e, f); these are likely mineral aggregates as *S. putrefaciens* are much larger than these structures (Derby and Hammer, 1931). As with GR-Si M, cytochrome C spectra (Fig. 6h) were found frequently with Raman spectroscopy for GR+Si M, and cytochrome C and green rust were the only identifiable spectra for both GR+Si M and GR-Si M samples. A fine acicular morphology was also seen on the SEM (Fig. 6d) for GR+Si M but could not be identified via Raman. On SEM-EDS, the iron-silica ratio for the platy clusters was 0.9 when accounting for magnesium substitutions ((Fe+Mg):Si). The capsule-shaped morphology had a (Fe+Mg):Si of 1.9, while the acicular structures had a (Fe+Mg):Si ratio of 2.3 (Table 5). All three had similar carbon and oxygen content (Table 5).
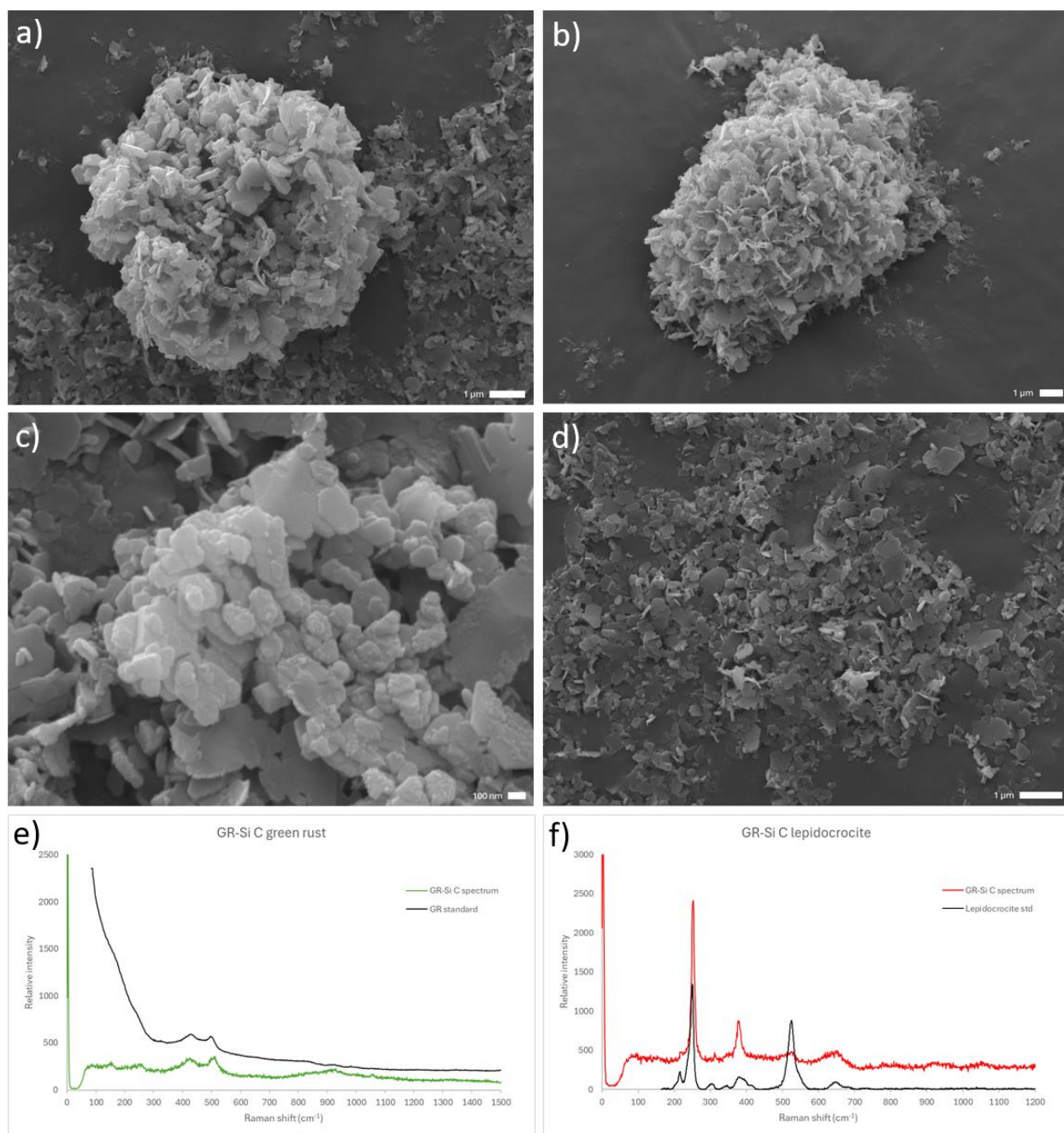
Figure 3   SEM and Raman spectroscopy data for the control experiment without silica (GR-Si C) after aging at room temperature for 15 days. Green rust was abundant, often forming loose aggregates (a, b) or swathes of degrading plates (d), and this morphology identification was corroborated by Raman data (e). Spherules resembling siderite were also seen (c). Lepidocrocite spectra were detected by Raman (f).
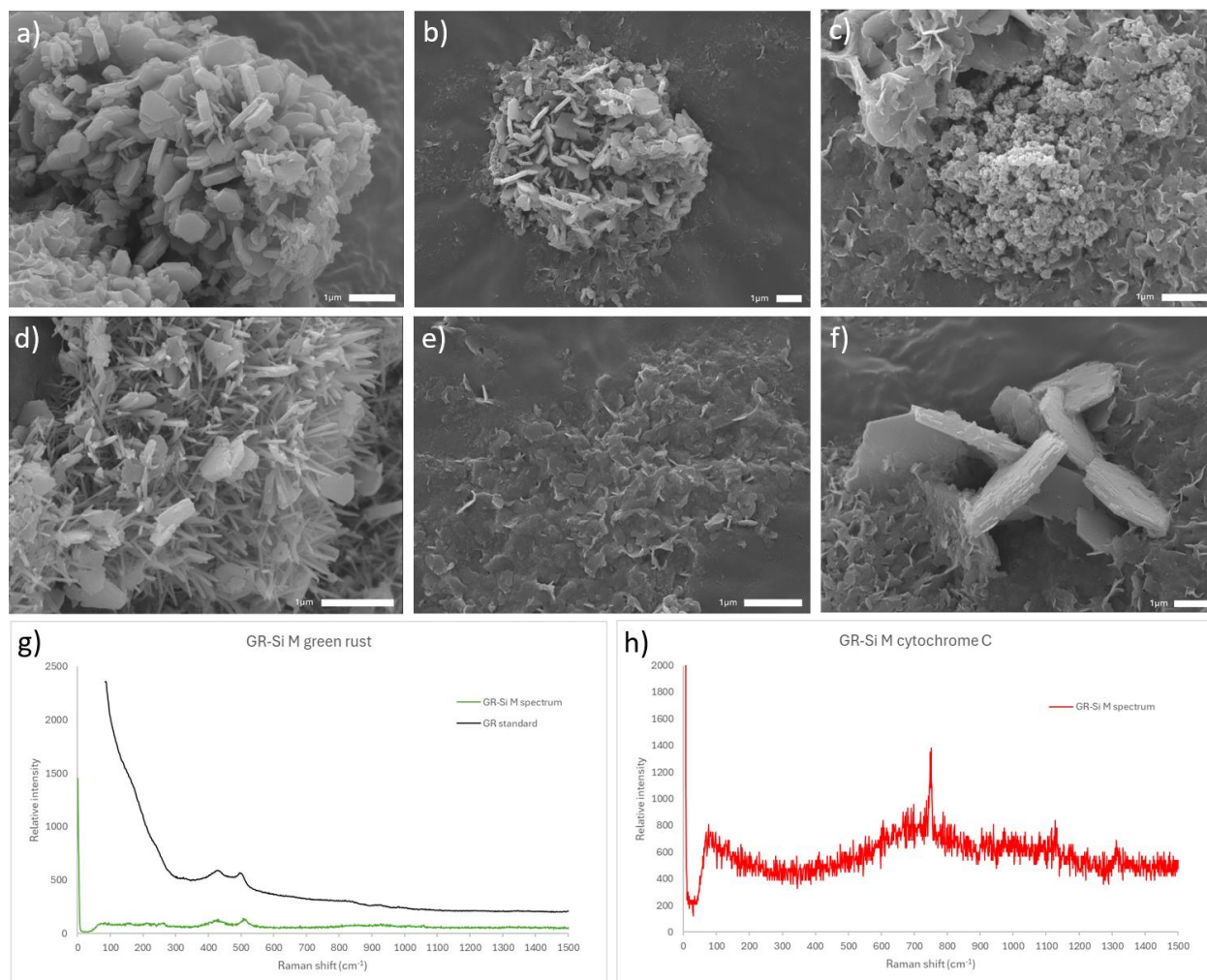
Figure 4 SEM and Raman spectroscopy data for the microbial treatments without silica (GR-Si M) after aging at room temperature for 15 days. Green rust hexagons were visible throughout the SEM images (a-f) and in Raman spectra as well (g). While no *S. putrefaciens* were seen on the SEM at this stage, the Raman microprobe picked up many spectra for cytochrome C (h), a common indicator of biological material. Spherules resembling early siderite (c) and an unknown acicular morphology (d) were also captured on the SEM but were not detected via Raman.
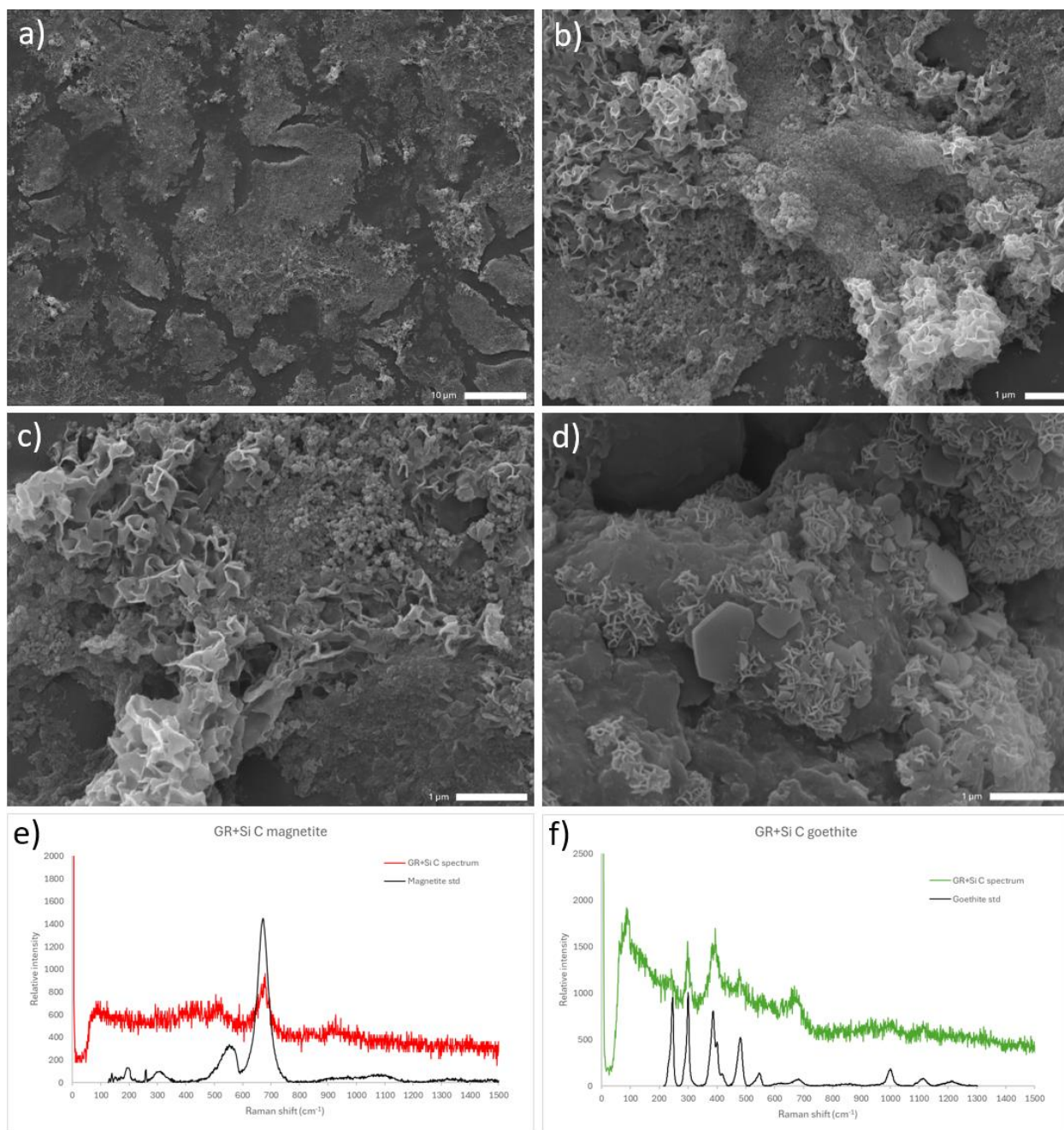
Figure 5   SEM and Raman spectroscopy data for the control treatment with silica (GR+Si C) after aging at room temperature for 15 days. The dominant morphologies seen on SEM were large curling plates and small platy clusters (both shown in b and c). A few green rust hexagons were also found (d). Raman analysis identified magnetite (e) and goethite (f).
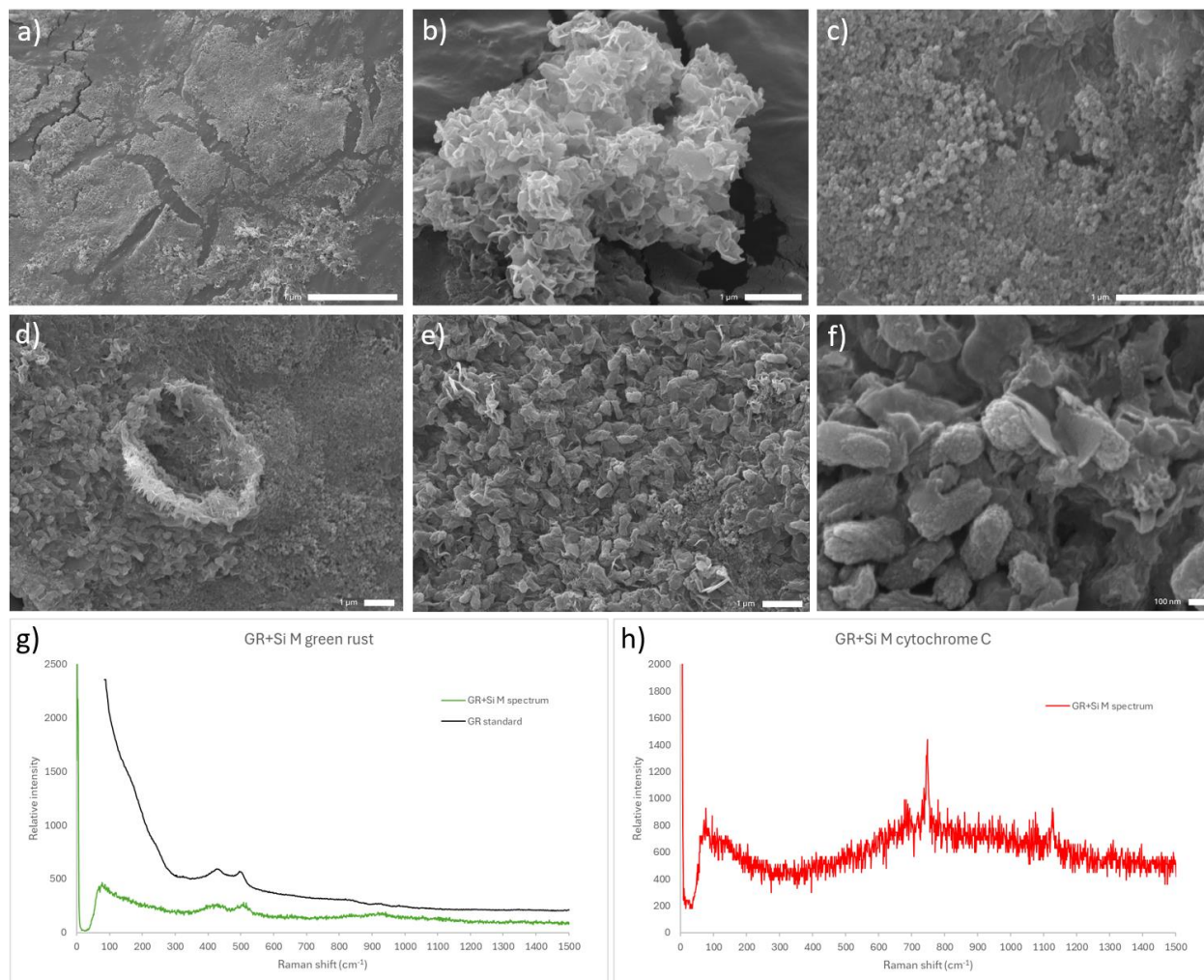
Figure 6 SEM and Raman spectroscopy data for the microbial treatments with silica (GR+Si M) after aging at room temperature for 15 days. Large curling plates (a, b) and small platy clusters (c) were the dominant morphologies. An unknown acicular morphology was again seen on SEM (d) and not identified by Raman, and a capsule-shaped morphology resembling microbes but too small to be *S. putrefaciens* is shown in e) and f).

3.3 Hydrothermally aged experimental precipitates

3.3.1   *Green rust without silica*

After 15 days of room temperature aging and 10 days of aging at 80°C, the GR-Si C sample contained aggregates of a large platy structure resembling chukanovite (Fig. 7a-c), an Fe(II) hydroxycarbonate $Fe_2(OH)_2CO_3$. This iron hydroxycarbonate was also identified on the Raman microprobe (Fig. 7g). Large spheres that appeared to be transforming into cubes were abundant in SEM images throughout the sample (Fig. 7d, e) with smaller spheres nearby (Fig. 7d). We also observed platy clusters (Fig. 7f). Raman spectroscopy identified spectra containing purely siderite peaks (Fig. 7h) or a mix of siderite and magnetite (Fig. 7i). The sphere-cube combinations had an average carbon content of 40%, oxygen 54.9%, and total iron 2.6%, while the platy clusters had relatively more oxygen and iron, at 34.6% C, 58.1% O, and 5.5% Fe (Table 5).

After hydrothermal aging, microbes were clearly visible in SEM images of the GR-Si M samples (Fig. 8a, b, d, e) and we measured cytochrome C spectra on the Raman microprobe (Fig. 8g). The microbes appeared to be encrusted in a mineral layer putatively identified as siderite based on SEM morphology and Raman spectra containing peaks for both cytochrome C and siderite (Fig. 8h). Green rust hexagons (Fig. 8c) and spheres identified as putative siderite were also seen on SEM (Fig. 8e, f). Raman spectra containing peaks for siderite and magnetite were seen as well, although the cubic structure characteristic of magnetite was not seen on SEM. We obtained SEM-EDS spectra for the hexagons, spheres, curling plates, and putative encrusted microbial phases (Table 5). The hexagons, spheres, and curling plates all had C and O percentages in the 40-50% range, with varying iron levels, while the proposed microbial forms had a much higher C content of 78.2% and O of only 19.9%.

3.3.2   *Green rust with silica*

In the hydrothermally aged GR+Si C precipitate, small platy clusters and curling plates were the main morphologies seen on SEM (Fig. 9a-d). We also observed a sheetlike morphology (Fig. 9c) that was less prevalent. The (Fe+Mg):Si ratios for the platy clusters and sheets were both 1. Raman spectra for GR+Si C at this timepoint were tentative matches for magnetite (Fig. 9e) and goethite (Fig. 9f).

In the GR+Si M precipitates, small platy clusters (Fig. 10a-c) and larger aggregates of curling plates (Fig. 10c) were again the dominant morphologies after hydrothermal aging. No green rust was seen on the SEM or Raman and no microbial forms were seen on the SEM, but cytochrome C spectra were seen on the Raman spectroscope (Fig. 10g), as well as a spectrum containing cytochrome C peaks and some other unidentifiable peaks (Fig. 10h). Sheetlike structures were once again present amongst the clusters and curling plates (Fig. 10b, d, e). We also found two spheres (Fig. 10d, e) that looked very different from the spheres seen in the GR-Si precipitates (ex. Fig. 8). Despite their similar morphology, the (Fe+Mg):Si ratio for the left and right spheres differed dramatically and were 49.3 and 7.3, respectively. The platy clusters, curling plates, and sheet morphologies had respective (Fe+Mg):Si of 1.1, 1.0, and 1.1 (Table 5). All phases of this treatment measured on SEM-EDS had similar C and O content in the 50% and 30% range, respectively, except the curling plates, which had more O than C (Table 5).
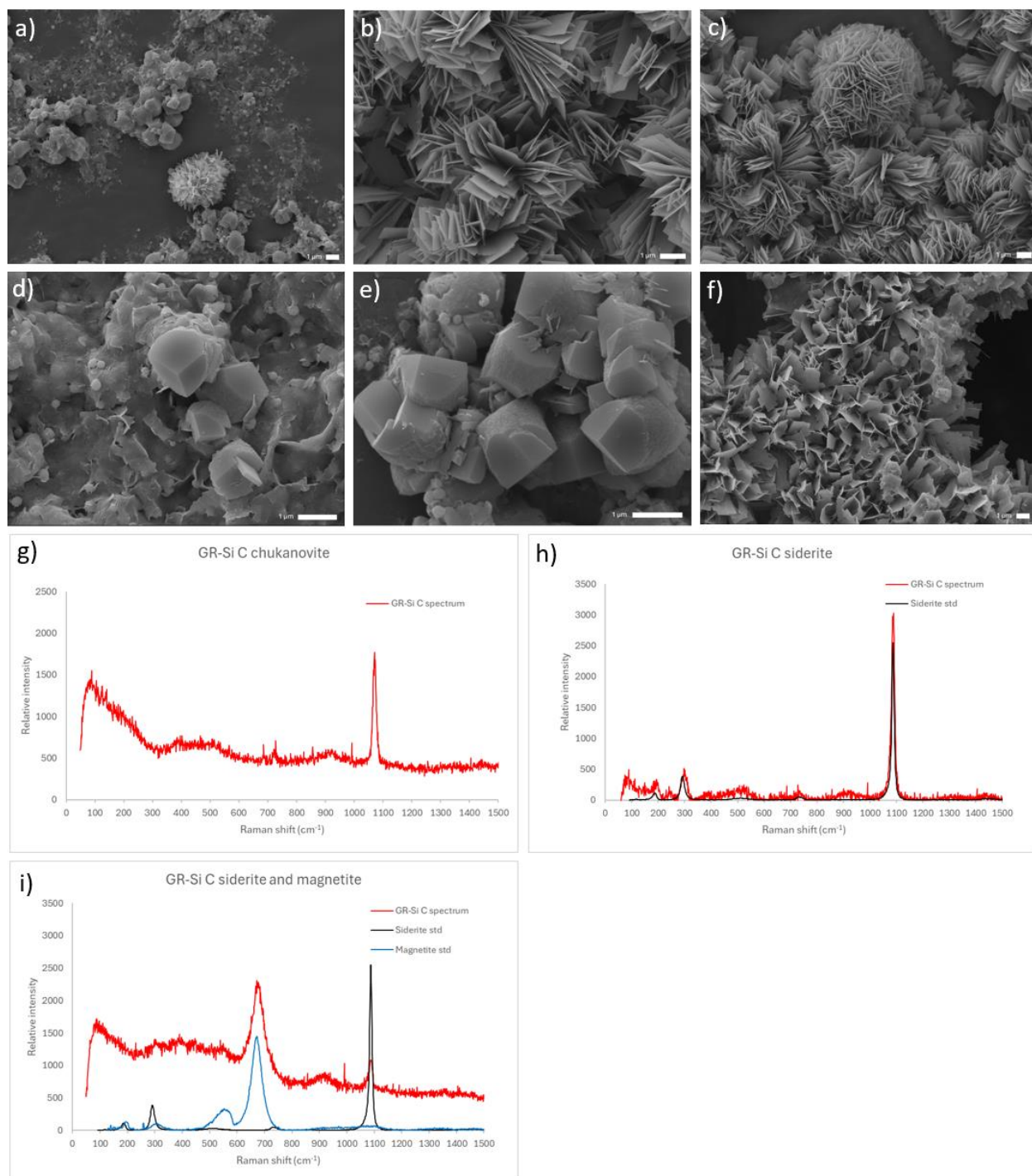
Figure 7   SEM and Raman spectroscopy data for the control treatment without silica (GR-Si C) after hydrothermal aging. The dominant morphologies in this sample after hydrothermal aging were large platy aggregates (a-c) identified on Raman as chukanovite (g), and siderite spheres transforming into magnetite cubes (d, e) as supported by Raman spectra with strong matches for siderite (h) and a combination of siderite and magnetite peaks (i).
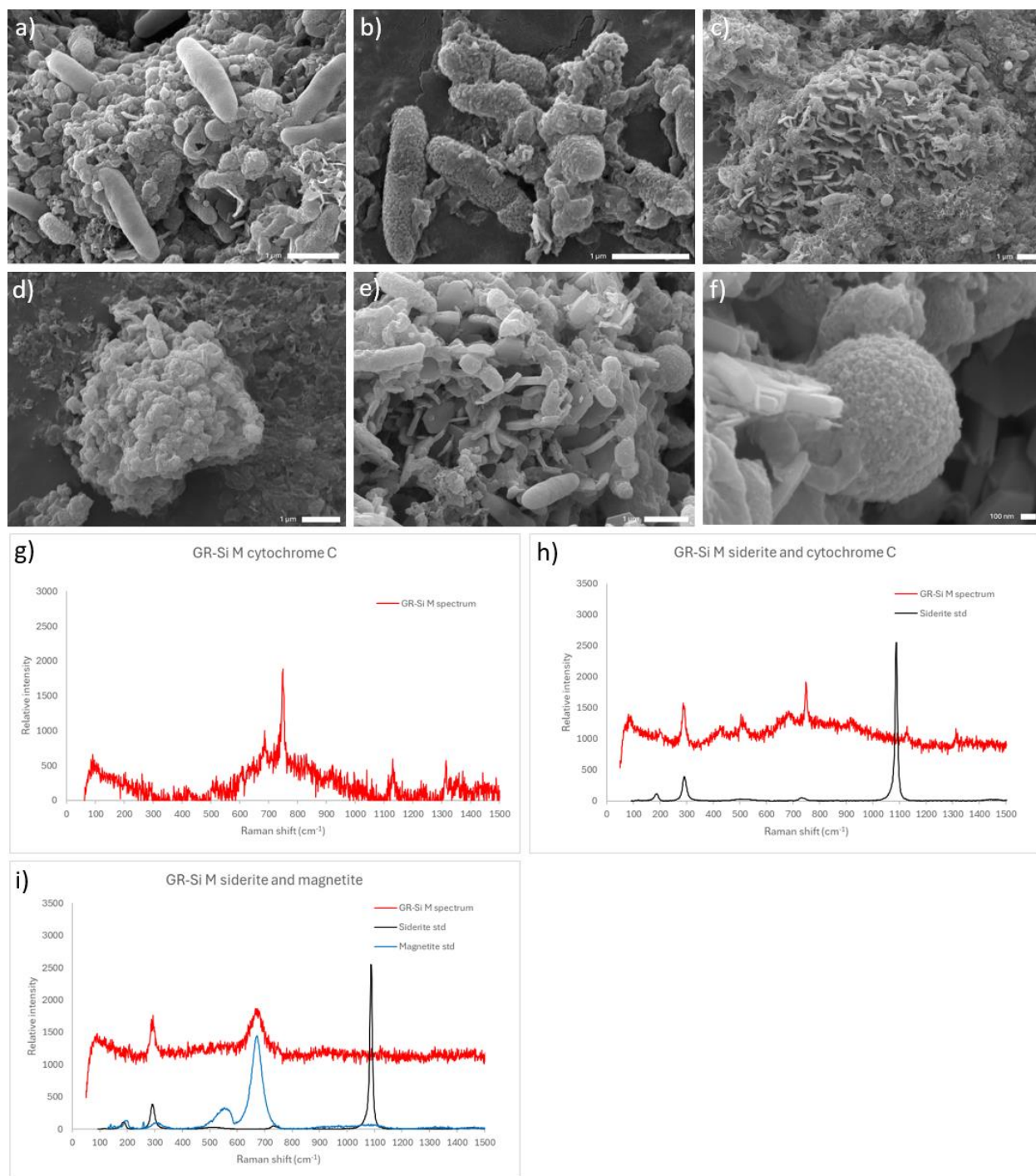
Figure 8   SEM and Raman spectroscopy data for the microbial treatments without silica (GR-Si M) after hydrothermal aging. *S. putrefaciens* was clearly visible throughout the SEM samples (a, b, d, e) and detected on Raman via cytochrome C (g, h) and they appear to be encrusted in a mineral coating resembling siderite (b), supported by Raman spectra containing peaks for both cytochrome C and siderite (h). Siderite spheres (c, e, f) and clusters (d) were also found, and some green rust hexagons were still present (c, e). Magnetite peaks were also detected on Raman in combination with siderite (i).
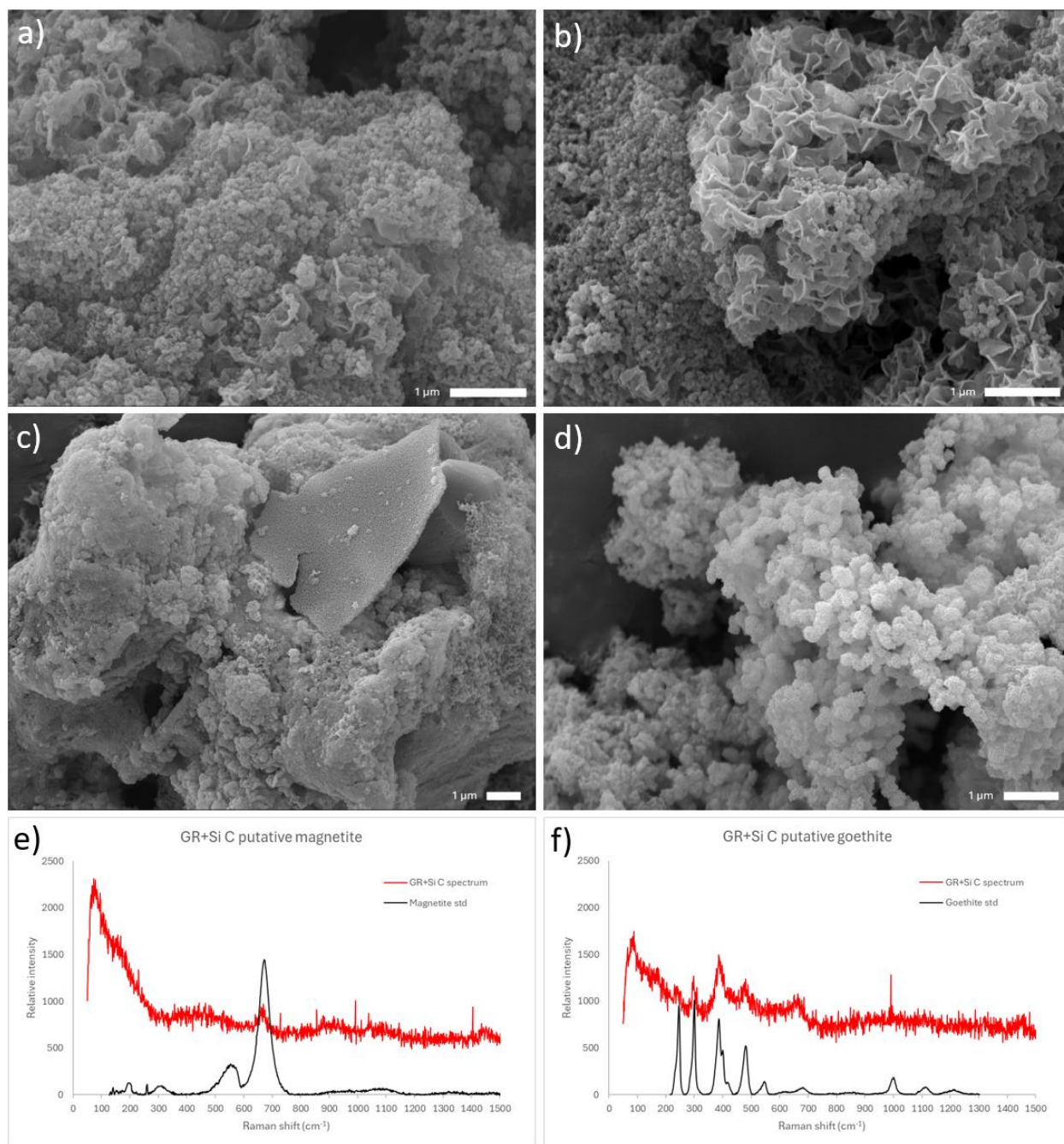
Figure 9 SEM and Raman spectroscopy data for the control treatment with silica (GR+Si C) after hydrothermal aging. Large curling plates, small platy clusters, and sheets dominated (a-d). No other notable morphology was seen, but magnetite and goethite were detected via Raman (e, f).
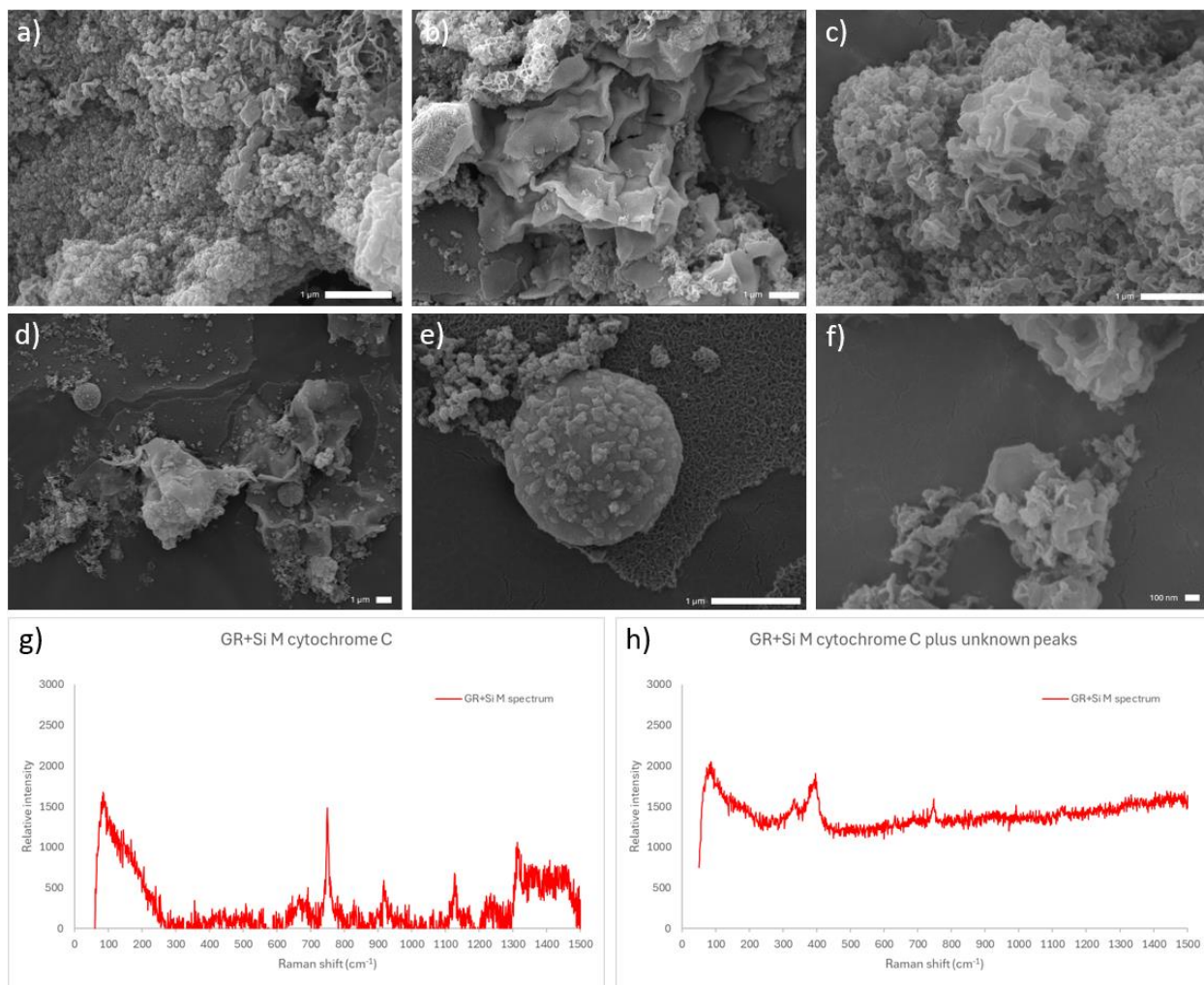
Figure 10   SEM and Raman spectroscopy data for the microbial treatments with silica after hydrothermal aging. Large curling plates, small platy clusters, and sheets remain the dominant morphologies (a-e), with a few anomalies including two large spheres (d, e) and a few rare hexagons (f). None of these morphologies were identifiable via Raman, with only cytochrome C being detected.
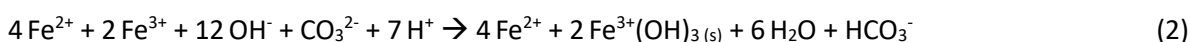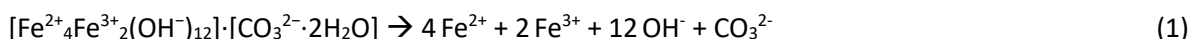
4   Discussion

4.1   Overview

Our primary aims with this study were to 1) explore the effects of microbial iron reduction on carbonate green rust and 2) explore the effects of silica on green rust transformation. Microbes are thought to have lived in Archean oceans and sediments when BIFs were forming (Schopf et al. 1993, 2018) and thus could have had a profound effect on BIF genesis and diagenesis, especially if these microbes were capable of iron metabolism. BIFs are rich in silicate minerals, supporting the idea that silica concentrations were higher in Archean oceans and porewaters than their modern counterparts (Siever, 1992; Maliva et al. 2005; Stefurak et al 2015). However, silica is also known to stabilize green rust and slow its transformation into other mineral phases (Feng et al. 2015; Sahoo et al. 2011). This quandary prompted us to investigate the dynamics between green rust and silica and how they affect BIF mineral formation in the presence and absence of microbial iron reduction.
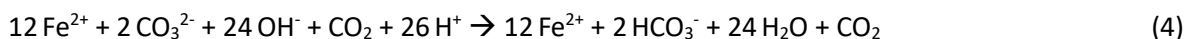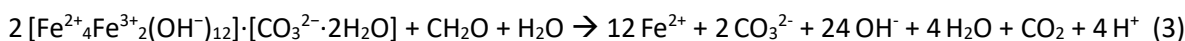
4.2   Synthesis

4.2.1   Solution chemistry

The trends of solution pH, Fe(II), and Fe(T) all increasing over the first three days (Fig. 1a, c, d) can be explained via both biotic and abiotic pathways. For example, in the abiotic control the instability of green rust causes some of its Fe^{2+}, Fe^{3+}, and CO_3^{2-} constituents to dissolve (Reaction 1). The ions released subsequently react in circumneutral water (Reaction 2). Fe^{3+} forms insoluble complexes with hydroxide ions, thus removing OH^- from solution and decreasing the pH. However, the presence of carbonate and bicarbonate ions helps buffer the water (1-2). Fe(T) in solution, including the Fe(II) fraction, increased alongside this dissolution reaction and rising pH.

$$[Fe^{2+}_4Fe^{3+}_2(OH^-)_{12}]\cdot[CO_3^{2-}\cdot 2H_2O] \rightarrow 4\,Fe^{2+} + 2\,Fe^{3+} + 12\,OH^- + CO_3^{2-} \tag{1}$$

$$4\,Fe^{2+} + 2\,Fe^{3+} + 12\,OH^- + CO_3^{2-} + 7\,H^+ \rightarrow 4\,Fe^{2+} + 2\,Fe^{3+}(OH)_{3\,(s)} + 6\,H_2O + HCO_3^- \tag{2}$$

In the microbe-containing treatments, *S. putrefaciens* began reducing the solid Fe(III) in carbonate green rust to soluble Fe(II), increasing the Fe(II) and therefore also Fe(T) in solution (simplified version shown in Reaction 3). This reaction also consumes H^+ ions by releasing hydroxide ions at circumneutral pH, thereby increasing the pH in a similar manner to the reactions that follow the dissolution of green rust (Reaction 4).

$$2\,[Fe^{2+}_4Fe^{3+}_2(OH^-)_{12}]\cdot[CO_3^{2-}\cdot 2H_2O] + CH_2O + H_2O \rightarrow 12\,Fe^{2+} + 2\,CO_3^{2-} + 24\,OH^- + 4\,H_2O + CO_2 + 4\,H^+ \tag{3}$$

$$12\,Fe^{2+} + 2\,CO_3^{2-} + 24\,OH^- + CO_2 + 26\,H^+ \rightarrow 12\,Fe^{2+} + 2\,HCO_3^- + 24\,H_2O + CO_2 \tag{4}$$

The pH continued to increase for all six solutions through day 5 (Fig. 1a). Subsequently, the pH plateaued in the GR-Si solutions, decreased in one GR+Si microbial solution (GR+Si 2), and increased slightly in the other two GR+Si experiments (Fig. 1a). Both Fe(II)-carbonate precipitation and Fe(II)-silicate precipitation should lower pH. Silicate precipitation would uptake hydroxide ions and release protons to form a phase similar to $Fe(II,III)_3Si_2O_5(OH)_4$, while iron carbonate precipitation would release protons from bicarbonate (HCO_3^-) ions at circumneutral pH to precipitate $Fe(II)CO_3^{2-}$. The solution Fe(II) and Fe(T) seemed to stabilize after 7 days, suggesting that the degradation of green rust – microbial or abiotic – was roughly in balance with iron precipitation.

The initial drop in silica concentration down from 1 mM to 0.2-0.4 mM on day 1, increase days 1-3, large fluctuations days 3-10, and stabilization days 10-15 suggests that most interactions between silica and green rust or other newly forming phases occurred between days 3 and 10, but does not provide insights into the details of those interactions. In the GR-Si treatment, the slight increase in silica levels across the 15 days is likely due to the reaction vessels being made of borosilicate glass, which would have leached low levels of silica into the solutions over time.

4.2.2   EDS data

All of the spectra we acquired through SEM-EDS were dominated by carbon and oxygen, with carbon content being the most abundant element in most samples (Table 5). The actual carbon content of the mineral phases is lower than these data suggest due to the samples being mounted on carbon tape, but there is still likely a large carbon portion from the precipitate itself, which fits with the carbonate component of green rust and siderite. The C, O, and Fe percentages seen for hexagons across sample conditions are similar to those seen for the initial green rust precipitate (Table 5), further supporting the SEM morphological and Raman spectral data pointing to green rust. In the GR-Si precipitates, all phases except those identified as putative microbes had lower C content and higher O content than the initial green rust, while still having C > O. The only phases to have higher O than C levels were the sphere-cube combinations identified as siderite transforming into magnetite, and platy aggregates identified as chukanovite. These deviations fit with the characteristics of their proposed sources. Magnetite is composed entirely of mixed-valence iron and oxygen, which explains the lower C content of putative siderite-magnetite compared with just siderite or green rust. Chukanovite contains a greater proportion of oxygen than carbon (Pekov et al. 2007), again explaining the higher O % relative to other phases. At the other end of the scale, the putative cells measured on SEM-EDS had significantly more carbon and less oxygen than any other phase. Microbial cells have a high carbon content, averaging at 53% C (Lee and Fuhrman, 1987); when combined with the carbon tape, this explains the high percentage of 78.1% C for this phase. The biggest deviations in total Fe content from the initial green rust (3.8%) were again the putative microbes (0.8% Fe), consistent with the microbial rather than mineral nature of this material; the spheres identified as siderite (7.5% Fe), which is not surprising because fully formed siderite is nearly 50% Fe(II); and the platy aggregates IDed as chukanovite (5.5% Fe), another high-Fe mineral. The sphere-cube transition phase only had 2.6% Fe across six point spectra, which is unexpected since siderite and magnetite are both iron-rich. Given more time to crystallize, this value may have increased.

For the GR+Si precipitates, C concentrations were higher in microbial treatments than in the abiotic controls and were comparable with the original green rust C level, especially after hydrothermal aging (Table 5). O concentrations were above C in all three abiotic phases we measured, even in phases that looked similar to those found in the microbial treatments. Assuming the carbon tape accounts for similar C% with or without microbes, these results suggest that either less reduction or more CO_3^{2-} removal occurred in the abiotic precipitates, or a combination of the two. Both explanations are plausible since *S. putrefaciens* would be actively reducing the Fe(III) in green rust without targeting the CO_3^{2-}, while an abiotic transformation would dissociate Fe(II), Fe(III), and CO_3^{2-} without bias. Si concentrations varied across the GR+Si experiments, with no clear pattern between biotic and abiotic treatments or before and after hydrothermal aging (Table 5). We saw more stability in (Fe+Mg):Si ratios, however, especially after hydrothermal aging, with values of 0.9-1 for (Fe+Mg):Si in all three abiotic phases and 1-1.1 for (Fe+Mg):Si in all GR+Si M phases except the two anomalous spheres. The high Fe and low Si content of

these spheres suggests that very different minerals were forming at these sites than the rest of the GR+Si phases, but their scarcity indicates that this phase is not as representative of green rust transformation in a silica-rich environment.

4.2.3 Precipitate products of room temperature aging

After 15 days of aging at room temperature, we observed persistent hexagons in both the GR-Si M and GR-Si C precipitates (Figs. 3 and 4). These were confirmed to be green rust by Raman spectroscopy and morphological comparison with the initial green rust precipitate. This suggests that under the anoxic AAS experimental conditions, both biotically and abiotically mediated green rust transformations are slow. However, we did see some changes from initial green rust. In both GR-Si M and GR-Si C, the hexagons formed aggregates, and another mineral phase consisting of tiny spheres had appeared. Based on previous experiments (not shown) and literature regarding the transformation of green rust into siderite (Halevy et al. 2017), we suspected that this new phase was siderite, but could not confirm it via Raman spectroscopy. These similarities between the microbial and abiotic control experiments suggested that there is no discernible difference between biotic and abiotic transformation of green rust at room temperature, at least at this time scale. A minor difference observed between the two experimental conditions was a needle-like acicular phase in GR-Si M (Fig. 4d) and not in GR-Si C. Many iron minerals, such as goethite or lepidocrocite, can have that morphology, and this phase could not be identified via Raman spectroscopy, so no conclusions could be made. Interestingly, we did find Raman spectra for lepidocrocite, but only in the GR-Si C precipitate, which did not exhibit this acicular morphology (Fig. 3f). Cytochrome C spectra were the only spectra other than green rust that we obtained for the GR-Si M precipitates (Fig. 4h) and were not seen in the GR-Si C precipitate. Cytochrome C spectra are a hallmark of biological material (Strekas and Spiro, 1972), confirming that although microbes were not visible on SEM, they were present in the microbial experiments and had not contaminated the abiotic control.

In the GR+Si set of experiments, similar phases appeared once again in the microbial and control precipitates. Both exhibited a phase of curling plate aggregates and flatter sheets of tiny platy clusters (Figs. 5 and 6). The curling plates resembled degrading green rust hexagons, and green rust Raman spectra found in the microbial treatment suggest that this may be the case; undegraded hexagons were too low in abundance to explain these spectra. We found an acicular phase in GR+Si M, but as with the GR-Si M condition, the only Raman spectra we got were for green rust and cytochrome C, so this phase could neither be identified nor confirmed to be the same as the acicular phase seen in the GR-Si M precipitates. Despite the morphological similarities between the biotic and abiotic phases seen on SEM, magnetite and goethite spectra were found on Raman for GR+Si C, suggesting that different phases were forming in the abiotic precipitate but were not yet visible.

After this room-temperature aging period, we saw major morphological differences between the GR+Si and GR-Si conditions. While Raman spectra only showed green rust and cytochrome C for microbial treatments regardless of the presence of silica, the phases seen on SEM were completely different (Figs. 4 and 6). We found few morphological differences between the microbial and abiotic control treatments within the GR-Si and GR+Si groups. At room temperature, therefore, silica appeared to have a clear effect on green rust transformation, while DIR did not seem to produce notably different results from abiotic green rust dissolution.

4.2.4   Precipitate products of hydrothermal aging

After the precipitates were aged for 10 days at 80°C, differences between treatments became more pronounced. Within the GR-Si M experiments, microbial cells were visible throughout the precipitates, corroborated by cytochrome C spectra (Fig. 8). The microbes appeared to be mineral-encrusted, and Raman spectra with a combination of cytochrome C and siderite peaks suggested this mineral to be siderite. This finding is in keeping with literature reports of microbes enhancing siderite nucleation under similar conditions (Posth et al. 2010). Phases resembling green rust hexagons and siderite spheres were also present but could not be confirmed on Raman. SEM-EDS data for the spheres supported them being an iron carbonate based on C, O, and Fe concentrations. Unlike at the room-temperature aged stage, the GR-Si C phases stood in stark contrast with the GR-Si M treatment in both morphology and spectroscopy. The spheric-cubic combination and the large platy aggregates (Fig. 7) were unlike anything seen in the GR-Si M precipitates (Fig. 8). We identified the platy aggregates as chukanovite based on Raman spectra matching chukanovite and the higher O and Fe content relative to initial green rust. The sphere-cubes looked like siderite spheres transforming into magnetite cubes, and Raman spectra containing peaks for both minerals supported this, along with literature documentation of siderite to magnetite transformations (Kaufman et al. 1990; Johnson et al. 2008; Rasmussen and Muhling, 2018). We also found Raman spectra containing peaks for both siderite and magnetite in GR-Si M precipitates despite seeing only spheres and no magnetite-like cubes. These similar mixed spectra suggest that the same mineral phases were forming in both biotic and abiotic conditions, albeit more slowly on the biotic side. Similar results were found by Han et al. (2020), who saw abiotic transformation of ferrihydrite occur faster than biotic transformation by iron-reducing microbes.

The GR+Si precipitates appeared to have changed little after hydrothermal aging; the curling plates, platy clusters, and sheetlike morphologies were still present in both the microbial and control experiments (Figs. 9 and 10). We found the same magnetite and goethite Raman spectra for the GR+Si C and cytochrome C for GR+Si M that we saw before aging at 80°C, but no green rust spectra, suggesting that some unseen changes might have occurred with green rust transformation. The (Fe+Mg):Si ratio of 1 ± 0.1 for most phases in the GR+Si condition is lower than the ratio of 1.5 seen in greenalite and higher than the 0.75 ratio found in minnesotaite $(Fe^{2+},Mg)_3Si_4O_{10}(OH)_2$, another iron silicate prominent in BIFs. However, this approximately 1:1 ratio of iron and magnesium to silica is consistent with precursor iron silicates formed in prior studies (Tosca et al. 2016, Hinz et al 2023). Further aging to increase mineral crystallization would provide more conclusive information on whether one or multiple of these 1:1 Fe:Si phases would develop into greenalite or minnesotaite. The two spherelike morphologies seen in GR+Si M after aging at 80°C had (Fe+Mg):Si ratios very far from 1:1, at 49:1 and 7:1 for Fig. 10d and 10e, respectively, suggesting that very different mineral phases were forming here. However, only two such spheres were found and were only a few microns apart, so cannot be considered representative of green rust transformation in the presence of *S. putrefaciens* and 1 mM Si. These ratios are more consistent with silica adsorbing onto iron oxides rather than forming an iron-silica phase. Again, further aging would provide more information on these spheres.

After 10 days of aging at 80°C, we saw a clear difference between DIR and abiotic green rust transformation in the GR-Si condition with SEM morphology, SEM-EDS atomic ratios, and Raman spectra. We did not see a significant difference between DIR and abiotic green rust alteration in the GR+Si condition at the morphological or atomic ratio levels but did see differences in Raman spectra. Finally, we saw the biggest morphological, atomic, and spectral differences between the GR+Si and GR-Si

conditions, regardless of biotic or abiotic conditions. We observed that green rust will transform into siderite and subsequently magnetite in the absence of silica, whether mediated by DIR or abiotic reactions. Aging at 80°C had the desired effect of accelerating crystallization in the GR-Si conditions, with defined mineral phases appearing particularly in the control experiment. Minimal crystallization was visible in the GR+Si condition, suggesting that silica slows down green rust transformation even under simulated diagenetic conditions.

4.3   Effects of silica on green rust transformation

Overall, our results suggest that the presence of silica has a profound effect on the transformation of green rust in Archean ocean conditions. In all GR+Si precipitates, silica appeared to have an inhibitory effect on green rust transformation. This was particularly pronounced after hydrothermal aging. At day 15, the microbial and control treatments resembled each other within the GR-Si and within GR+Si conditions. At day 25, GR-Si M and GR-Si C precipitates had clear morphological and spectrographic differences, while the GR+Si M and GR+Si C precipitates appeared nearly identical morphologically and differed only spectrographically, with no strong Raman peaks to speak of in either condition. These results suggest that the presence of silica in this green rust-AAS environment inhibited siderite, magnetite, and other iron oxides or carbonates such as chukanovite from forming. Given more time, however, some or all of these minerals might still have formed, as suggested by the few spectra weakly resembling magnetite (Fig. 9e) or goethite found in the GR+Si C precipitate at day 15 (Fig. 5f) and day 25 (Fig. 9f). Previous studies have found that silica provides a stabilizing effect by inhibiting oxidation of green rust into other mineral species (Feng et al 2015; Sahoo et al 2011), which fits with the results seen in this study both before and after hydrothermal aging. Presence or absence of *S. putrefaciens* did not seem to affect the level of inhibition exacted by silica, with similar morphologies of little to no crystal structure dominating in both the microbial and control treatments (Figs. 9 and 10). As explored by O'Loughlin et al. (2010), the adsorption of silica onto mineral phases like green rust can block iron-reducing microbes' access to the minerals, inhibiting reduction.

4.4   Implications for geochemical conditions during BIF genesis

In this study, our experiments formed siderite and magnetite from green rust via both dissimilatory iron reduction and abiotic pathways under anoxic Archean ocean conditions. The conversion occurred more completely in the abiotic conditions, but given more time to crystallize, Raman spectra indicate that siderite and magnetite were forming via DIR as well. Green rust transformation to siderite and magnetite, respectively a prominent Fe(II) carbonate and Fe(II,III) oxide found in BIFs, only occurred in the absence of silica. Under conditions containing 1 mM dissolved silica, which is more representative of Archean seawater, we saw no clear mineralization of siderite, magnetite, or any other mineral. Iron and silica coprecipitated together in ~1:1 (Fe+Mg):Si ratios in DIR and abiotic experiments, and if aged for longer, may have developed into greenalite or minnesotaite, common BIF iron silicates. Raman data suggested that magnetite and goethite, another Fe(II,III) oxide, were also beginning to form. These results suggest that green rust transforms into iron carbonates and oxides when silica is absent and into iron silicates – and maybe oxides, but not carbonates – when silica is present. This raises the question of if, as generally inferred, silica was abundant in Archean oceans (Siever, 1992; Maliva et al. 2005; Stefurak et al 2015), how did BIF iron carbonates form under these silica-rich conditions? BIFs contain layers of alternating silica-rich and silica-poor minerals for reasons that are not fully understood (Bekker et al.

2010, 2014). A potential explanation for these layers and for the seemingly paradoxical results of this study is that when silica concentrations were high in and around Archean sediments, iron silicates and mineralized silica (chert) would be the main minerals to form from the microbial or abiotic degradation of green rust, creating a silica-rich BIF layer. As more iron silicates formed, silica would drop below saturation levels, creating an environment in which green rust could transform into iron carbonates and oxides. This would form a silica-poor BIF layer rich in carbonates and oxides below the silica-rich horizon. This model is supported by previous observations suggesting that chert horizons form at the sediment-water interface (Krapež et al. 2003). Furthermore, our work is consistent with experiments showing that iron silicate phases form under Archean conditions supersaturated for silica and that newly formed greenalite limited silica still in solution from becoming saturated (Tosca et al. 2016).

4.5 Future directions

This study built upon previous work by Nims and Johnson (2022) that explored the products of ferrihydrite DIR in Archean seawater conditions. We looked at DIR of carbonate green rust under these same conditions, with a few modifications: we removed Ca^{2+} from seawater chemistry, increased the starting concentration of total iron, and started with a ~3:1 ratio of Fe(II):Fe(III) instead of an Fe(III) phase. We made these changes because we wanted to obtain DIR products that did not contain fully oxidized iron phases or calcium carbonates and that did include iron carbonates. We achieved these aims and were able to study the transformation of green rust into Fe(II) carbonates, Fe(II,III) oxides, and Fe-Si coprecipitates that showed the potential to become iron silicates. One outstanding question following this study is: if aged hydrothermally for a longer period of time, would the difference between DIR and abiotic products of green rust transformation become more pronounced? In the GR-Si condition, the answer appears to be yes; the precipitates in microbe-containing experiments were barely distinguishable from the abiotic control after 15 days of aging at room temperature, but were markedly different following 10 days of aging at 80°C. The answer is less clear in the presence of 1 mM Si, but the detection of magnetite and goethite in Raman spectroscopy data in only the control treatment suggests that eventually there would also be differences between DIR and abiotic products of green rust transformation in the GR+Si condition. This leads to the second outstanding question: given enough time to react, would green rust undergo the same transformations independent of silica? That is, are the same reactions occurring in both the GR+Si and GR-Si conditions, just at different rates? Based on our results, the answer to this question seems to be no. Rather than simply altering rate of transformation, silica seems to be affecting which minerals form, with no siderite or other iron carbonates seen when silica is present. Both of these questions could be answered more fully with a follow-up experiment that includes a longer hydrothermal aging period to allow for more crystallization of mineral phases. Further exploration of the products of green rust transformation under these conditions would improve our understanding of the involvement of DIR in BIF mineral formation, whether carbonate green rust is a likely precursor to BIF mineral phases, and how silica impacted mineralization in Archean seawater conditions. Together, this information will help to determine whether a record of early life on Earth has been recorded in Archean BIFs, and whether that information can be used as a biosignature to find life beyond our planet.

References

Abdelmoula, M., Trolard, F., Bourrié, G., Génin, J.-M.R., 1998. Evidence for the Fe(II)-Fe(III) Green Rust "Fougerite" Mineral Occurrence in a Hydromorphic Soil and Its Transformation with Depth. Hyperfine Interactions 112, 235–238. https://doi.org/10.1023/A:1010802508927

Balch, W.E., Wolfe, R.S., 1976. New approach to the cultivation of methanogenic bacteria: 2-mercaptoethanesulfonic acid (HS-CoM)-dependent growth of Methanobacterium ruminantium in a pressureized atmosphere. Appl Environ Microbiol 32, 781–791. https://doi.org/10.1128/aem.32.6.781-791.1976

Bae, S., Lee, W., 2013. Biotransformation of lepidocrocite in the presence of quinones and flavins. Geochimica et Cosmochimica Acta 114, 144–155. https://doi.org/10.1016/j.gca.2013.03.041

Bekker, A., Planavsky, N.J., Krapež, B., Rasmussen, B., Hofmann, A., Slack, J.F., Rouxel, O.J., Konhauser, K.O., 2014. 9.18 - Iron Formations: Their Origins and Implications for Ancient Seawater Chemistry, in: Holland, H.D., Turekian, K.K. (Eds.), Treatise on Geochemistry (Second Edition). Elsevier, Oxford, pp. 561–628. https://doi.org/10.1016/B978-0-08-095975-7.00719-1

Bekker, A., Slack, J.F., Planavsky, N., Krapež, B., Hofmann, A., Konhauser, K.O., Rouxel, O.J., 2010. Iron Formation: The Sedimentary Product of a Complex Interplay among Mantle, Tectonic, Oceanic, and Biospheric Processes*. Economic Geology 105, 467–508. https://doi.org/10.2113/gsecongeo.105.3.467

Bernal, J.D., Megaw, H.D., Fowler, R.H., 1997. The function of hydrogen in intermolecular forces. Proceedings of the Royal Society of London. Series A - Mathematical and Physical Sciences 151, 384–420. https://doi.org/10.1098/rspa.1935.0157

Beukes, N.J., Gutzmer, J., 2008. Origin and Paleoenvironmental Significance of Major Iron Formations at the Archean-Paleoproterozoic Boundary, in: Hagemann, S., Rosière, C.A., Gutzmer, J., Beukes, N.J. (Eds.), Banded Iron Formation-Related High-Grade Iron Ore. Society of Economic Geologists, p. 0. https://doi.org/10.5382/Rev.15.01

Braterman, P.S., Cairns-Smith, A.G., Sloper, R.W., 1983. Photo-oxidation of hydrated Fe2+—significance for banded iron formations. Nature 303, 163–164. https://doi.org/10.1038/303163a0

Chorney, A.P., Chemtob, S.M., 2023. Iron precipitation under controlled oxygen flow: Mineralogical implications for BIF precursors in the Archean ocean. Chemical Geology 618, 121279. https://doi.org/10.1016/j.chemgeo.2022.121279

Cornell, R.M., Giovanoli, R., Schindler, P.W., 1987. Effect of silicate species on the transformation of ferrihydrite into goethite and hematite in alkaline media. Clays Clay Miner. 35, 21–28. https://doi.org/10.1346/CCMN.1987.0350103

Cosmidis, J., Benzerara, K., Morin, G., Busigny, V., Lebeau, O., Jézéquel, D., Noël, V., Dublet, G., Othmane, G., 2014. Biomineralization of iron-phosphates in the water column of Lake Pavin (Massif Central, France). Geochimica et Cosmochimica Acta 126, 78–96. https://doi.org/10.1016/j.gca.2013.10.037

Craddock, P.R., Dauphas, N., 2011. Iron and carbon isotope evidence for microbial iron respiration throughout the Archean. Earth and Planetary Science Letters 303, 121–132. https://doi.org/10.1016/j.epsl.2010.12.045

Derby, H.A, Hammer, B.W., 1931. Bacteriology of butter IV. Bacteriological studies on surface taint butter. Iowa Agricultural Experimental Station Research Bulletin 145, 387-416.

Etique, M., Jorand, F.P.A., Ruby, C., 2016. Magnetite as a precursor for green rust through the hydrogenotrophic activity of the iron-reducing bacteria Shewanella putrefaciens. Geobiology 14, 237–254. https://doi.org/10.1111/gbi.12170

Feng, X., Wang, X., Zhu, M., Koopal, L.K., Xu, H., Wang, Y., Liu, F., 2015. Effects of phosphate and silicate on the transformation of hydroxycarbonate green rust to ferric oxyhydroxides. Geochimica et Cosmochimica Acta 171, 1–14. https://doi.org/10.1016/j.gca.2015.08.020

Fischer, W.W., Knoll, A.H., 2009. An iron shuttle for deepwater silica in Late Archean and early Paleoproterozoic iron formation. Geol Soc America Bull preprint, 1. https://doi.org/10.1130/B26328.1

Halevy, I., Alesker, M., Schuster, E.M., Popovitz-Biro, R., Feldman, Y., 2017. A key role for green rust in the Precambrian oceans and the genesis of iron formations. Nature Geosci 10, 135–139. https://doi.org/10.1038/ngeo2878

Halevy, I., Bachan, A., 2017. The geologic history of seawater pH. Science 355, 1069–1071. https://doi.org/10.1126/science.aal4151

Han, X., Tomaszewski, E.J., Sorwat, J., Pan, Y., Kappler, A., Byrne, J.M., 2020. Effect of Microbial Biomass and Humic Acids on Abiotic and Biotic Magnetite Formation. Environ. Sci. Technol. 54, 4121–4130. https://doi.org/10.1021/acs.est.9b07095

Heimann, A., Johnson, C.M., Beard, B.L., Valley, J.W., Roden, E.E., Spicuzza, M.J., Beukes, N.J., 2010. Fe, C, and O isotope compositions of banded iron formation carbonates demonstrate a major role for dissimilatory iron reduction in ~2.5 Ga marine environments. Earth and Planetary Science Letters 294, 8–18. https://doi.org/10.1016/j.epsl.2010.02.015

Hinz, I.L., Nims, C., Theuer, S., Templeton, A.S., Johnson, J.E., 2021. Ferric iron triggers greenalite formation in simulated Archean seawater. Geology 49, 905–910. https://doi.org/10.1130/G48495.1

James, H.L., 1954. Sedimentary facies of iron-formation. Economic Geology 49, 235–293. https://doi.org/10.2113/gsecongeo.49.3.235

Jiang, C.Z., Tosca, N.J., 2019. Fe(II)-carbonate precipitation kinetics and the chemistry of anoxic ferruginous seawater. Earth and Planetary Science Letters 506, 231–242. https://doi.org/10.1016/j.epsl.2018.11.010

Johnson, C.M., Beard, B.L., Klein, C., Beukes, N.J., Roden, E.E., 2008. Iron isotopes constrain biologic and abiologic processes in banded iron formation genesis. Geochimica et Cosmochimica Acta 72, 151–169. https://doi.org/10.1016/j.gca.2007.10.013

Johnson, J.E., Muhling, J.R., Cosmidis, J., Rasmussen, B., Templeton, A.S., 2018. Low-Fe(III) Greenalite Was a Primary Mineral From Neoarchean Oceans. Geophysical Research Letters 45, 3182–3192. https://doi.org/10.1002/2017GL076311

Jones, A.M., Collins, R.N., Rose, J., Waite, T.D., 2009. The effect of silica and natural organic matter on the Fe(II)-catalysed transformation and reactivity of Fe(III) minerals. Geochimica et Cosmochimica Acta 73, 4409–4422. https://doi.org/10.1016/j.gca.2009.04.025

Kappler, A., Pasquero, C., Konhauser, K.O., Newman, D.K., 2005. Deposition of banded iron formations by anoxygenic phototrophic Fe(II)-oxidizing bacteria. Geology 33, 865–868. https://doi.org/10.1130/G21658.1

Kaufman, A.J., Hayes, J.M., Klein, C., 1990. Primary and diagenetic controls of isotopic compositions of iron-formation carbonates. Geochimica et Cosmochimica Acta 54, 3461–3473. https://doi.org/10.1016/0016-7037(90)90298-Y

Kester, D.R., Duedall, I.W., Connors, D.N., Pytkowicz, R.M., 1967. Preparation of Artificial Seawater1. Limnology and Oceanography 12, 176–179. https://doi.org/10.4319/lo.1967.12.1.0176

Klein, C., Beukes, N.J., 1989. Geochemistry and sedimentology of a facies transition from limestone to iron-formation deposition in the early Proterozoic Transvaal Supergroup, South Africa. Economic Geology 84, 1733–1774. https://doi.org/10.2113/gsecongeo.84.7.1733

Konhauser, K.O., Amskold, L., Lalonde, S.V., Posth, N.R., Kappler, A., Anbar, A., 2007. Decoupling photochemical Fe(II) oxidation from shallow-water BIF deposition. Earth and Planetary Science Letters 258, 87–100. https://doi.org/10.1016/j.epsl.2007.03.026

Konhauser, K.O., Planavsky, N.J., Hardisty, D.S., Robbins, L.J., Warchola, T.J., Haugaard, R., Lalonde, S.V., Partin, C.A., Oonk, P.B.H., Tsikos, H., Lyons, T.W., Bekker, A., Johnson, C.M., 2017. Iron formations: A global record of Neoarchaean to Palaeoproterozoic environmental history. Earth-Science Reviews 172, 140–177. https://doi.org/10.1016/j.earscirev.2017.06.012

Krapež, B., Barley, M.E., Pickard, A.L., 2003. Hydrothermal and resedimented origins of the precursor sediments to banded iron formation: sedimentological evidence from the Early Palaeoproterozoic Brockman Supersequence of Western Australia. Sedimentology 50, 979–1011. https://doi.org/10.1046/j.1365-3091.2003.00594.x

Kröner, A., 1985. Evolution of the Archean continental crust. Archean crustal evolution.

Kump, L.R., Seyfried, W.E., 2005. Hydrothermal Fe fluxes during the Precambrian: Effect of low oceanic sulfate concentrations and low hydrostatic pressure on the composition of black smokers. Earth and Planetary Science Letters 235, 654–662. https://doi.org/10.1016/j.epsl.2005.04.040

Lee, S., Fuhrman, J.A., 1987. Relationships between Biovolume and Biomass of Naturally Derived Marine Bacterioplankton. Applied and Environmental Microbiology 53, 1298–1303. https://doi.org/10.1128/aem.53.6.1298-1303.1987

Lovley, D.R., Phillips, E.J.P., 1988. Novel Mode of Microbial Energy Metabolism: Organic Carbon Oxidation Coupled to Dissimilatory Reduction of Iron or Manganese. Applied and Environmental Microbiology 54, 1472–1480. https://doi.org/10.1128/aem.54.6.1472-1480.1988

Lyons, T.W., Reinhard, C.T., Planavsky, N.J., 2014. The rise of oxygen in Earth's early ocean and atmosphere. Nature 506, 307–315. https://doi.org/10.1038/nature13068

Maliva, R.G., Knoll, A.H., Simonson, B.M., 2005. Secular change in the Precambrian silica cycle: Insights from chert petrology. GSA Bulletin 117, 835–845. https://doi.org/10.1130/B25555.1

Myers, C.R., Nealson, K.H., 1988. Bacterial manganese reduction and growth with manganese oxide as the sole electron acceptor. Science 240, 1319–1321. https://doi.org/10.1126/science.240.4857.1319

Nims, C., Johnson, J.E., 2022. Exploring the secondary mineral products generated by microbial iron respiration in Archean ocean simulations. Geobiology 20, 743–763. https://doi.org/10.1111/gbi.12523

O'Loughlin, E.J., Gorski, C.A., Flynn, T.M., Scherer, M.M., 2019. Electron Donor Utilization and Secondary Mineral Formation during the Bioreduction of Lepidocrocite by Shewanella putrefaciens CN32. Minerals 9, 434. https://doi.org/10.3390/min9070434

O'Loughlin, E.J., Gorski, C.A., Scherer, M.M., Boyanov, M.I., Kemner, K.M., 2010. Effects of Oxyanions, Natural Organic Matter, and Bacterial Cell Numbers on the Bioreduction of Lepidocrocite (γ-FeOOH) and the Formation of Secondary Mineralization Products. Environ. Sci. Technol. 44, 4570–4576. https://doi.org/10.1021/es100294w

Pekov, I., Perchiazzi, N., Merlino, S., Kalachev, V., Merlini, M., Zadov, A., 2007. Chukanovite, Fe 2 (CO 3)(OH) 2 , a new mineral from the weathered iron meteorite Dronino. European Journal of Mineralogy - EUROPEAN J MINERAL 19, 891–898. https://doi.org/10.1127/0935-1221/2007/0019-1767

Percak-Dennett, E.M., Beard, B.L., Xu, H., Konishi, H., Johnson, C.M., Roden, E.E., 2011. Iron isotope fractionation during microbial dissimilatory iron oxide reduction in simulated Archaean seawater. Geobiology 9, 205–220. https://doi.org/10.1111/j.1472-4669.2011.00277.x

Posth, N.R., Huelin, S., Konhauser, K.O., Kappler, A., 2010. Size, density and composition of cell–mineral aggregates formed during anoxygenic phototrophic Fe(II) oxidation: Impact on modern and ancient environments. Geochimica et Cosmochimica Acta 74, 3476–3493. https://doi.org/10.1016/j.gca.2010.02.036

Posth, N.R., Köhler, I., D. Swanner, E., Schröder, C., Wellmann, E., Binder, B., Konhauser, K.O., Neumann, U., Berthold, C., Nowak, M., Kappler, A., 2013a. Simulating Precambrian banded iron formation diagenesis. Chemical Geology, Special Issue dedicated to H.D. Holland: Evolution of the atmosphere and ocean through time 362, 66–73. https://doi.org/10.1016/j.chemgeo.2013.05.031

Rasmussen, B., Krapež, B., Meier, D.B., 2014. Replacement origin for hematite in 2.5 Ga banded iron formation: Evidence for postdepositional oxidation of iron-bearing minerals. GSA Bulletin 126, 438–446. https://doi.org/10.1130/B30944.1

Rasmussen, B., Muhling, J.R., 2018. Making magnetite late again: Evidence for widespread magnetite growth by thermal decomposition of siderite in Hamersley banded iron formations. Precambrian Research 306, 64–93. https://doi.org/10.1016/j.precamres.2017.12.017

Rasmussen, B., Muhling, J.R., Krapež, B., 2021. Greenalite and its role in the genesis of early Precambrian iron formations – A review. Earth-Science Reviews 217, 103613. https://doi.org/10.1016/j.earscirev.2021.103613

Rasmussen, B., Muhling, J.R., Suvorova, A., Krapež, B., 2017. Greenalite precipitation linked to the deposition of banded iron formations downslope from a late Archean carbonate platform. Precambrian Research 290, 49–62. https://doi.org/10.1016/j.precamres.2016.12.005

Rasmussen, B., Muhling, J.R., Suvorova, A., Krapež, B., 2016. Dust to dust: Evidence for the formation of "primary" hematite dust in banded iron formations via oxidation of iron silicate nanoparticles. Precambrian Research 284, 49–63. https://doi.org/10.1016/j.precamres.2016.07.003

Ruby, C., Aïssa, R., Géhin, A., Cortot, J., Abdelmoula, M., Génin, J.-M., 2006. Green rusts synthesis by coprecipitation of FeII–FeIII ions and mass-balance diagram. Comptes Rendus Geoscience, Les hydroxydes ferrosiques, les rouilles vertes et la fougérite dans le cycle biogéochimique du fer 338, 420–432. https://doi.org/10.1016/j.crte.2006.04.008

Sahoo, G., Fujieda, S., Shinoda, K., Yamaguchi, S., Korosaki, M., Suzuki, S., 2011. Influence of silicon species on the transformation of green rust I(Cl–) in aqueous solution by oxidation. Corrosion Science 53, 4001–4009. https://doi.org/10.1016/j.corsci.2011.08.003

Salas, E.C., Berelson, W.M., Hammond, D.E., Kampf, A.R., Nealson, K.H., 2009. The Influence of Carbon Source on the Products of Dissimilatory Iron Reduction. Geomicrobiology Journal 26, 451–462. https://doi.org/10.1080/01490450903060806

Schopf, J.W., 1993. Microfossils of the Early Archean Apex Chert: New Evidence of the Antiquity of Life. Science 260, 640–646.

Schopf, J.W., Kitajima, K., Spicuzza, M.J., Kudryavtsev, A.B., Valley, J.W., 2018. SIMS analyses of the oldest known assemblage of microfossils document their taxon-correlated carbon isotope compositions. Proceedings of the National Academy of Sciences 115, 53–58. https://doi.org/10.1073/pnas.1718063115

Siever, R., 1992. The silica cycle in the Precambrian. Geochimica et Cosmochimica Acta 56, 3265–3272. https://doi.org/10.1016/0016-7037(92)90303-Z

Stefurak, E.J.T., Lowe, D.R., Zentner, D., Fischer, W.W., 2015. Sedimentology and geochemistry of Archean silica granules. GSA Bulletin 127, 1090–1107. https://doi.org/10.1130/B31181.1

Stookey, L.L., 1970. Ferrozine---a new spectrophotometric reagent for iron. Anal. Chem. 42, 779–781. https://doi.org/10.1021/ac60289a016

Strekas, T.C., Spiro, T.G., 1972. Cytochrome C: Resonance Raman spectra. Biochimica et Biophysica Acta (BBA) - Protein Structure 278, 188–192. https://doi.org/10.1016/0005-2795(72)90121-3

Strickland, J.D.H., Parsons, T.R., 1972. A Practical Handbook of Seawater Analysis, 2nd edition. https://doi.org/10.25607/OBP-1791

Sumoondur, A., Shaw, S., Ahmed, I., Benning, L.G., 2008. Green rust as a precursor for magnetite: an in situ synchrotron based study. Mineral. mag. 72, 201–204. https://doi.org/10.1180/minmag.2008.072.1.201

Sun, S., Konhauser, K.O., Kappler, A., Li, Y.-L., 2015. Primary hematite in Neoarchean to Paleoproterozoic oceans. GSA Bulletin 127, 850–861. https://doi.org/10.1130/B31122.1

Tosca, N.J., Guggenheim, S., Pufahl, P.K., 2016. An authigenic origin for Precambrian greenalite: Implications for iron formation and the chemistry of ancient seawater. GSA Bulletin 128, 511–530. https://doi.org/10.1130/B31339.1

Tosca, N.J., Jiang, C.Z., Rasmussen, B., Muhling, J., 2019. Products of the iron cycle on the early Earth. Free Radical Biology and Medicine, Early Life on Earth and Oxidative Stress 140, 138–153. https://doi.org/10.1016/j.freeradbiomed.2019.05.005

Viollier, E., Inglett, P.W., Hunter, K., Roychoudhury, A.N., Van Cappellen, P., 2000. The ferrozine method revisited: Fe(II)/Fe(III) determination in natural waters. Applied Geochemistry 15, 785–790. https://doi.org/10.1016/S0883-2927(99)00097-9

Walker, J.C.G., 1984. Suboxic diagenesis in banded iron formations. Nature 309, 340–342. https://doi.org/10.1038/309340a0

Widdel, F., Kohring, G.-W., Mayer, F., 1983. Studies on dissimilatory sulfate-reducing bacteria that decompose fatty acids. Arch. Microbiol. 134, 286–294. https://doi.org/10.1007/BF00407804

Widdel, F., Schnell, S., Heising, S., Ehrenreich, A., Assmus, B., Schink, B., 1993. Ferrous iron oxidation by anoxygenic phototrophic bacteria. Nature 362, 834–836. https://doi.org/10.1038/362834a0

Wu, L., Beard, B.L., Roden, E.E., Johnson, C.M., 2009. Influence of pH and dissolved Si on Fe isotope fractionation during dissimilatory microbial reduction of hematite. Geochimica et Cosmochimica Acta 73, 5584–5599. https://doi.org/10.1016/j.gca.2009.06.026

Zegeye, A., Bonneville, S., Benning, L.G., Sturm, A., Fowle, D.A., Jones, C., Canfield, D.E., Ruby, C., MacLean, L.C., Nomosatryo, S., Crowe, S.A., Poulton, S.W., 2012. Green rust formation controls nutrient availability in a ferruginous water column. Geology 40, 599–602. https://doi.org/10.1130/G32959.1

Zegeye, A., Mustin, C., Jorand, F., 2010. Bacterial and iron oxide aggregates mediate secondary iron mineral formation: green rust versus magnetite. Geobiology 8, 209–222. https://doi.org/10.1111/j.1472-4669.2010.00238.x

Zhou, A., Templeton, A.S., Johnson, J.E., 2024. Dissolved silica affects the bulk iron redox state and recrystallization of minerals generated by photoferrotrophy in a simulated Archean ocean. Geobiology 22, e12587. https://doi.org/10.1111/gbi.12587

Supplementary material

Table S1   Trace minerals

Chemical name	MW (g/mol)	[ ] in 100X stock (g/L)	Formula	Vendor/Cat #	Final [ ] in AAS medium (µM)
Nitrilotriacetic acid	191.1	1.5	$C_6H_9NO_3$	Sigma N-9877	78.49
Magnesium sulfate heptahydrate	246.48	3	$MgSO_4\ 7H_2O$	Aldrich 23,039-1	121.71
Manganese sulfate monohydrate	169.02	0.5	$MnSO_4\ H_2O$	Aldrich 22,128-7	29.58
Sodium chloride	58.44	1	NaCl	Sigma S-3014	171.12
Ferrous sulfate heptahydrate	277.91	0.1	$FeSO_4\ 7H_2O$	Sigma F-8633	3.60
Calcium chloride dihydrate	146.99	0.1	$CaCl_2\ 2H_2O$	Sigma C-3881	6.80
Cobalt chloride hexahydrate	237.93	0.1	$CoCl_2\ 6H_2O$	Sigma C-3169	4.20
Zinc chloride	136.28	0.13	$ZnCl_2$	Sigma Z-3500	9.54
Cupric sulfate pentahydrate	249.68	0.01	$CuSO_4\ 5H_2O$	Sigma C-6283	0.40
Aluminum potassium disulfate dodecahydrate	474.38	0.01	$AlK(SO_4)_2\ 12H_2O$	Sigma A-7167	0.21
Boric acid	61.83	0.01	H_3BO_3	Sigma B-6768	1.62
Sodium molybdate dihydrate	241.95	0.025	$Na_2MoO_4\ 2H_2O$	Aldrich 22,184-8	1.03
Nickel chloride hexahydrate	237.60	0.024	$NiCl_2\ 6H_2O$	Sigma N-6136	1.01
Sodium tungstate	329.86	0.025	$Na_2WO_4\ 2H_2O$	Sigma S-0765	0.76

From Widdel et al. (1983).

Table S2   Vitamins

Chemical name	MW (g/mol)	[ ] in 1000X stock (g/L)	Formula	Vendor/Cat #	Final [ ] in AAS medium (µM)
D-biotin	244.3	0.002	$C_{10}H_{16}N_2O_3S$	Sigma B-4639	81.87
Folic acid	441.1	0.002	$C_{19}H_{19}N_7O_6$	Sigma F-7876	45.34
Pyridoxine HCl	205.6	0.010	$C_8H_{12}ClNO_3$	Sigma P-9755	486.38
Riboflavin	376.4	0.005	$C_{17}H_{20}N_4O_6$	Sigma R-4500	132.84
Thiamine HCl 1.0 H_2O	355.3	0.005	$C_{18}H_{18}Cl_2N_4OS$	Sigma T-4625	140.73
Nicotinic acid	123.1	0.005	$C_6H_5NO_2$	Sigma N-4126	406.17
D-pantothenic acid, hemicalcium salt	238.3	0.005	$C_9H_{16}NO_5\ ½Ca$	Sigma P-2250	209.82
B12	1355.4	0.0001	$C_{63}H_{88}CoN_{14}O_{14}P$	Sigma V-2876	0.74
P-aminobenzoic acid	137.13	0.005	$C_7H_7NO_2$	Sigma A-9878	364.62
Thioctic acid (α-lipoic acid)	206.3	0.005	$C_8H_{14}O_2S_2$	Sigma T-5625	242.37

From Balch and Wolfe (1976).

Table S3   **Amino acids**

	[ ] in 100X stock (g/L)	Vendor/Cat #	Final [ ] in AAS medium (mg/L)
L-glutamic acid	2	Sigma G-1251	2
L-arginine	2	Sigma A-3909	2
L-serine	2	Sigma S-4375	2

From Myers and Nealson (1990).